Article

Drug−Polymer Nanodroplet Formation and Morphology Drive Solubility Enhancement of GDC-0810

Kaylee E. Barr,□ Monica L. Ohnsorg,□ Lucy Liberman, Louis G. Corcoran, Apoorva Sarode, Karthik Nagapudi, Christina R. Feder, Frank S. Bates,* and Theresa M. Reineke*

Cite This: https://doi.org/10.1021/acs.bioconjchem.4c00018

Read Online

ACCESS | Metrics & More | Article Recommendations | Supporting Information

ABSTRACT: Nanodroplet formation is important to achieve supersaturation of active pharmaceutical ingredients (APIs) in an amorphous solid dispersion. The aim of the current study was to explore how polymer composition, architecture, molar mass, and surfactant concentration affect polymer−drug nanodroplet morphology with the breast cancer API, GDC-0810. The impact of nanodroplet size and morphology on dissolution efficacy and drug loading capacity was explored using polarized light microscopy, dynamic light scattering, and cryogenic transmission electron microscopy. Poly(N-isopropylacrylamide-stat-N,N-dimethylacrylamide) (PND) was synthesized as two linear derivatives and two bottlebrush derivatives with carboxylated or PEGylated end-groups. Hydroxypropyl methylcellulose acetate succinate grade MF (HPMCAS-MF) and poly(vinylpyrrolidone-co-vinyl acetate) (PVPVA) were included as commercial polymer controls. We report the first copolymerization synthesis of a PVPVA bottlebrush copolymer, which was the highest performing excipient in this study, maintaining 688 μg/mL GDC-0810 concentration at 60 wt % drug loading. This is likely due to strong polymer−drug noncovalent interactions and the compaction of GDC-0810 along the PVPVA bottlebrush backbone. Overall, it was observed that the most effective formulations had a hydrodynamic radius less than 25 nm with tightly compacted nanodroplet morphologies.
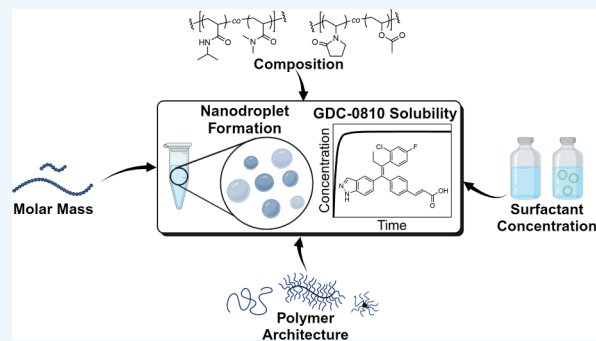
INTRODUCTION

Amorphous solid dispersions (ASDs), in which an active pharmaceutical ingredient (API) is molecularly dispersed within a polymer matrix, are among the most widely used methods to improve the oral bioavailability of APIs with poor aqueous solubility.[1−3] Standard commercial polymer excipients like hydroxypropyl methylcellulose acetate succinate (HPMCAS) and poly(vinylpyrrolidone-co-vinyl acetate) (PVPVA) have been formulated and FDA-approved, with a wide range of orally administered small molecule APIs.[4−10] Promoting the solubility of formulations containing higher drug loadings using well-designed polymer excipients is key to obtaining targeted drug concentrations high enough to achieve efficacy and reduce the pill burden on patients.[4,11−13] However, previous studies in this field have been limited by Edisonian trial-and-error testing of common commercially available polymer excipients to solubilize and deliver new drug candidates.[14]

Studies have shown that noncovalent interactions between the drug and polymer, along with the formation of nanostructures ranging in size from 10 to 1000 nm, mediate solubility enhancement and supersaturation maintenance.[15−20] These nanostructures are believed to be amorphous drug-rich nanodroplets surrounded by a drug-lean phase, which may be indicative of liquid−liquid phase-separation in the polymer−

drug nanostructure.[21−23] Previous work has shown how the formation of nanoparticles during dissolution correlates with the supersaturation and stabilization of high drug concentrations. This has been observed with HPMCAS spray-dried dispersions containing phenytoin[15] or telaprevir[24] as well as PVPVA formulations with ritonavir at low drug loadings.[25] In addition, polyacrylamide-based poly(N-isopropylacrylamide-stat-N,N-dimethylacrylamide) (PND) excipients have been shown to increase the solubility of Biopharmaceutics Classification System (BCS) Class II therapeutics beyond what is typically achievable with HPMCAS and PVPVA.[16,26] Hydrogen bonding between donor/acceptor moieties on the API and the N-isopropylacrylamide (NIPAm) repeat units in PND offered one mode of polymer−drug association. In addition, the statistical copolymer nature of PND-based excipients with 65−70 mol % NIPAm resulted in 3−4 repeat unit long blocks of NIPAm along the polymer chain that created a small hydrophobic pocket called an n-cluster.[27,28]
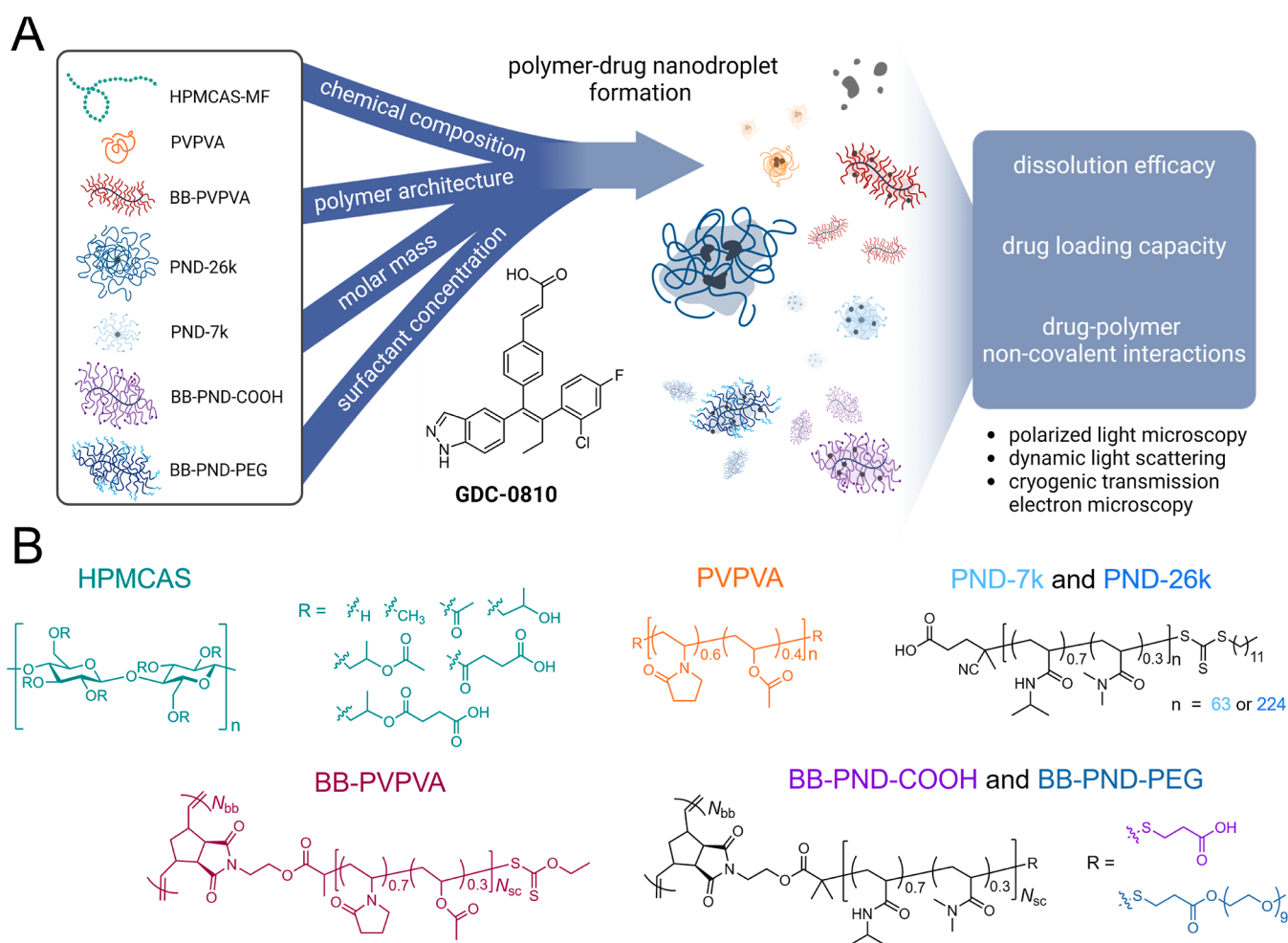
Figure 1. (A) Changing polymer chemical composition, architecture, molar mass, or surfactant concentration during dissolution led to different nanodroplet morphologies, dissolution efficacy, and drug loading capacity. This was explored using polarized light microscopy, DLS, and cryogenic transmission electron microscopy. (B) Chemical structures of HPMCAS, PVPVA, PND-7k, PND-26k, BB-PVPVA, BB-PND-COOH, and BB-PND-PEG.

These n-clusters may act as hydrophobic reservoirs for small molecule therapeutics and provide solubilization efficacy until fully saturated. To date, the chemical structures and mechanisms conducive to nanodroplet formation and drug solubility enhancement are yet to be fully understood, which are necessary for novel excipient discovery.

In addition to changing the polymer functional group composition, polymer architecture has also been demonstrated to influence solubilization efficacy during dissolution. Previous studies have evaluated the solubility enhancement of small molecule APIs with a variety of polymer architectures and self-assemblies, such as polymer nanogels,[29] micelles,[30−33] and bottlebrush polymers.[34,35] It was shown that increasing the micelle corona density of both PND copolymers and PNIPAm homopolymers enhanced drug−polymer noncovalent binding affinity, resulting in enhanced dissolution performance.[32,33] Bottlebrush polymers, which have side chains emanating radially from a polymer backbone, offer an alternative branched system where side chain density can be modulated synthetically. Previous work from our group demonstrated that PND bottlebrush polymers with carboxylated end-groups outperformed linear PND analogues of varying molar masses at enhancing the solubility of phenytoin at higher drug loadings (25 wt %) due to the unimolecular nature of

bottlebrush polymers in solution.[34,35] Despite individual studies, the influence of polymer functional group composition, molar mass, and architecture has not yet been thoroughly evaluated in tandem to determine how these factors influence drug−polymer nanostructure during dissolution.

Evaluating the polymer−drug nanostructures formed with different macromolecular chemistries and architectures will aid in the identification of structure−activity trends and new excipients for oral drug delivery. In this work, we selected the orally administered selective estrogen receptor degrader (SERD), GDC-0810, as the model API. GDC-0810 demonstrated oral bioavailability and activity in tamoxifen-resistant metastatic estrogen receptor positive breast cancer models.[36−40] It is an interesting model API for this study as it is both lipophilic and crystalline with a medium octanol-to-water partition coefficient ($\log P$) and high melting temperature (T_m), respectively (Figure S21B). This weak acid small molecule falls within BCS Class II due to its poor intrinsic solubility (<0.06 μg/mL).[41] GDC-0810 is an ideal model triphenylethylene-based SERD to understand how ASD formulations with excipients can be used to increase the solubility and oral bioavailability of future therapeutic derivatives.

Herein, we hypothesize that polymer composition, molar mass, architecture, and surfactant concentration will affect nanodroplet formation and GDC-0810 solubility enhancement. To test this hypothesis, we sought to understand how these variables dictate dissolution efficacy under different dissolution environments using a library of commercial and designer polymer excipients. We used our previously studied excipient, PND, and examined the role of polymer length *via* high- and low-molecular weight PND variants (*i.e.*, PND-26k and PND-7k, respectively) capable of self-assembly and the role of architecture *via* carboxylated and PEGylated PND bottlebrush excipients (*i.e.*, BB-PND-COOH and BB-PND-PEG, respectively)—as shown in Figure 1B. Moreover, we compared the role of chemistry in the bottlebrush architectures by synthesizing a bottlebrush derivative of PVPVA (*i.e.*, BB-PVPVA). This study reports the first copolymerization synthesis of a PVPVA bottlebrush copolymer. The synthesized polymer excipients were compared to commercial PVPVA and HPMCAS-MF excipients. The dissolution efficacy of these polymers formulated with GDC-0810 as ASDs was evaluated under non-sink dissolution conditions at pH 6.5 in aqueous maleate buffer (MB) with or without fasted state simulated intestinal fluid version 2 (FaSSIF-V2). We were able to draw conclusions about how polymer excipient chemical composition, architecture, molar mass, and surfactant concentration affect the polymer–drug nanodroplet formation using polarized light microscopy, dynamic light scattering (DLS), and cryogenic transmission electron microscopy to investigate the micro- and nanoscale features. While others have studied the importance of nanodroplet formation *via* liquid–liquid phase-separation for supersaturation in ASD formulations,[15,16,21,22,42,43] this study is the first to probe the factors that influence nanodroplet morphology and how these factors influence dissolution efficacy. Overall, this work shows that a broad range of polymer excipients efficiently promote solubilization of GDC-0810 and demonstrates key mechanisms important for next generation excipients to translate highly effective chemical structures with challenging physical properties into effective therapeutics.

◼ MATERIALS AND METHODS

Materials. All solvents purchased were of ACS grade, except those used for HPLC. The following reagents were used as received from Millipore Sigma, unless otherwise noted: ethanolamine (98%), toluene, acetone, potassium phosphate tribasic (98%), propanethiol (97%), carbon disulfide (CS$_2$, 99%), 2-bromo-2-methylpropionic acid (98%), 2-bromopropionic acid (99%), 4-dimethylaminopyridine (99%), hexanes, ethyl acetate, dichloromethane, NIPAm (97%), *N,N*-dimethylacrylamide (DMA, contains 500 ppm MEHQ as inhibitor, 99%), vinyl acetate (VA, contains 3−20 ppm hydroquinone as inhibitor, 99%), 1-vinyl-2-pyrrolidone (VP, contains sodium hydroxide as inhibitor, 99%), 2,2′-azobis(2-methylpropionitrile) (AIBN, 98%), 1,4-dioxane, methanol, dichloro[1,3-bis(2,4,6-trimethylphenyl)-2-imidazolidinylidene]-(benzylidene)bis(3-bromopyridine)ruthenium(II) (Grubbs Catalyst M300, G3), SiliaMetS-DMT (99%, molecular loading ≥0.50 mmol/g), 4-cyano-4-[(dodecylsulfanylthiocarbonyl)-sulfanyl]pentanoic acid (97%), triethylamine (≥99%), tetrahydrofuran (THF, anhydrous, contains 250 ppm BHT as inhibitor, ≥99.9%), tris(2-carboxyethyl)phosphine hydrochloride (TCEP, powder), *n*-propylamine (≥99%), poly(ethylene glycol) methyl ether acrylate (methyl-PEGA, average M_n =

480, contains 100 ppm BHT as inhibitor), *tert*-butyl acrylate (contains 10−20 ppm MEHQ as inhibitor, 98%), and trifluoroacetic acid (TFA, 99%).

GDC-0810 was used as received from Genentech, Inc. and stored in an amber bottle in the fridge (2−8 °C). *Cis*-5-norbornene-*exo*-2,3-dicarboxylic anhydride (>98%) was purchased from AOKChem. Diisopropylcarbodiimide (DIC, 97%) was purchased from Matrix Scientific. Potassium ethyl xanthogenate (97%) was purchased from Alfa Aesar. The commercial excipients, PVPVA and HPMCAS-MF (grade: micronized fine powder), were sourced from BASF and Shin-Etsu, respectively.

Dialysis tubing (regenerated cellulose, molecular weight cut off (MWCO) = 1, 6−8, and 12−14 kDa) was purchased from Spectra/Por, treated with a 0.1 wt % ethylenediaminetetraacetic acid (EDTA) solution, and stored in a ∼ 0.05 wt % sodium azide solution. The tubing was soaked and rinsed with Milli-Q water prior to use.

N,N-dimethylacrylamide, vinyl acetate, and 1-vinyl-2-pyrrolidone were passed through a small basic alumina column to remove inhibitors prior to use.

Chemical Synthesis and Characterization. The synthetic procedures, chemical schemes, NMR spectra, and SEC characterization results are provided in the Supporting Information.

Nuclear Magnetic Resonance (NMR). ^{1}H NMR spectroscopy experiments were performed using a Bruker Avance III HD 500 spectrometer equipped with a 5 mm Prodigy TCI cryoprobe with *z*-axis gradients at 22 °C using a 10 or 1 s relaxation delay for polymers or small molecules, respectively, and at least 32 transients without spinning to increase the signal-to-noise ratio in CDCl$_3$. ^{1}H NMR data was processed with Bruker TopSpin 3.5 pl 7 and MestReNova software.

Size Exclusion Chromatography (SEC). The polymers were analyzed on a size-exclusion chromatography with multiulti angle light scattering (SEC-MALS) instrument in DMF containing 0.05 M LiBr. The polymer sample was dissolved at a concentration of 3 mg/mL in the mobile phase and filtered through a 0.2 μm polytetrafluoroethylene (PTFE) membrane filter before injection into an Agilent Infinity 1200 HPLC system operating at 50 °C and 1.0 mL/min. The instrument was equipped with two Viscotek I-MBMMW-3078 columns, a Wyatt Optilab T-rEX differential refractive index detector, and a Wyatt HELEOS-II MALS detector.

Cloud Point Determination. Polymers were dissolved at 3 mg/mL in MB (pH 6.5) and filtered into glass ampules. The samples were heated in a temperature-controlled sample chamber at an approximate rate of 0.25 °C/min from room temperature (RT) to 50 or 70 °C. The optical transmittance of a 10 mW 633 nm HeNe laser was recorded on a photodiode detector during heating and cooling after passing through a neutral density filter followed by the sample. The cloud point was defined as the temperature at which the transmittance dropped below 80% from the normalized transmittance at RT.

Differential Scanning Calorimetry (DSC). DSC thermograms were collected with a Q1000 differential scanning calorimeter (TA Instruments, New Castle, DE) to determine the glass transition temperature (T_g) of polymer-only samples and select corresponding ASDs, as well as the melting temperature (T_m) of crystalline GDC-0810. The instrument was calibrated with a high-purity indium standard. Tzero aluminum pan lids were punctured with a needle to remove sample moisture during the first heat cycle, then samples were

carefully weighed into Tzero aluminum pans and hermetically sealed with a press. Samples were heated from −10 to 200 °C at a 3 °C/min rate, followed by cooling back to −10 °C and reheating to 200 °C at 3 °C/min under a continuous helium flow rate of 25 mL/min. Universal Analysis software (TA Instruments, New Castle, DE) was utilized to determine the T_g as the midpoint in the glass transition region or the T_m as the peak temperature of the melting endotherm.

Spray Drying. Each polymer excipient with a specified amount of GDC-0810 (25−60 wt %) was dissolved in methanol (20 mg/mL), except for HPMCAS-MF, which was dissolved in a 1:1 methanol/dichloromethane v/v solution. After thorough mixing, the sample was transferred to a 20 mL syringe. Using a Bend Research Mini Spray Dryer (Bend, OR), the sample was spray-dried using the following parameters: solution flow rate = 0.65 mL/min, inlet temperature = 85 °C, and nitrogen flow rate = 12.8 standard liters per minute. The powder was collected on filter paper and dried under a vacuum overnight before dissolution tests. The samples were stored in a vacuum desiccator at RT.

Non-sink Dissolution Experiments. Each dissolution experiment was run in triplicate. Spray-dried dispersions were weighed into 2 mL centrifuge tubes, to which MB (pH 6.5, 37 °C) with or without FaSSIF-V2 was added. The samples were vortexed for 1 min on a Vortex Genie 2 equipped with a Scientific Industries V524 Vertical Microtube Holder and placed in a VWR Digital Heatblock set to 37 °C. At 4 min, the samples were centrifuged for 1 min at 13,000 rpm (15,700g) in a preheated Eppendorf 5415R centrifuge to maintain temperature (Figure S22). After centrifugation, a 50 μL aliquot of each supernatant was taken, and then the samples were again vortexed for 1 min before returning to the hot plate. This process was repeated at 10, 20, 40, 90, 180, and 360 min.

Reversed-Phase High-Performance Liquid Chromatography (RP-HPLC). Each aliquot from the non-sink dissolution experiment was diluted with 450 μL of HPLC-grade methanol and filtered through a 0.2 μm PTFE membrane filter prior to analysis with reversed-phase HPLC (Agilent 1260 Quaternary Pump, 1260 Standard Autosampler, 1260 thermostatted column compartment, and 1260 Infinity Multiple Wavelength Detector VL) with a reversed-phase EC-C18 column (Poroshell 120, 4.6 × 50 mm, 2.7 μm from Agilent, USA). The following parameters were used: flow rate of 0.8 mL/min, injection volume of 3 μL, data acquisition time of 7 min, left column temperature of 40 °C, and a UV detection wavelength of 310 nm. A gradient method (see Table S2) using mobile phase A (88/12 (v/v) water/methanol with 0.1 vol % formic acid) and mobile phase B (88/12 (v/v) acetonitrile/methanol with 0.1 vol % formic acid) was used to analyze samples containing GDC-0810. Using these methods, GDC-0810 has an elution time of around 4.8 min. The HPLC calibration curve for GDC-0810 is provided in Figure S23.

Polarized Light Microscopy. Images were collected under normal dissolution conditions. However, each sample aliquot was taken after 30 s of agitation *via* vortex instead of centrifugation to gain a complete understanding regarding the presence of crystalline precipitates in the dissolution vial (Figure S24). At each time point, after suspending the sample with a vortex, a 20−50 μL aliquot was taken and deposited on a precleaned glass slide (3″ × 1″, Thermo Scientific), and the droplet was dispersed with a glass coverslip (24 × 40 mm², Fisher). The samples were imaged with a Lecia DM750P light microscope with cross polarizers at 10× magnification using a

Samsung Galaxy S10e phone camera attached to the microscope with a Celestron NexXY 3 Axis Universal Smartphone Adapter. The images of the pellet were taken at the respective time points after 1 min of centrifugation (13,000 rpm) after removing all the supernatant and transferring the remaining pellet onto a glass slide.

Dynamic Light Scattering (DLS). Select dissolution runs were conducted in FaSSIF-V2 and MB (pH 6.5) at a drug loading of 25 wt % GDC-0810. The FaSSIF-V2 and polymer-only samples at the relevant polymer concentration during dissolution were measured as t = 0 min control. FaSSIF-V2 or buffer only was added to the ASD, which was then vortexed and incubated at 37 °C. At 10, 40, 90, and 180 min, a 250 μL aliquot was taken of the supernatant and filtered through a 0.22 μm filter (to remove dust) into a separate microcentrifuge tube. From the sample time point, 200 μL was then pipetted into a 96-well glass bottom plate (Greiner Bio-One Sensoplate Microplate), and the DLS measurement was taken using the Wyatt Technologies DynaPro Plate Reader DLS (Figure S25). The DLS was heated to 37 °C, and each sample was measured 5 times for 10 s. The average autocorrelation function was analyzed with Wyatt technology's regularization fit, resulting in a particle size distribution plot for each time point (intensity vs R_h).

Cryogenic Transmission Electron Microscopy. Samples were prepared using a FEI Vitrobot Mark III automated vitrification device (Thermo Fisher Scientific, USA) on 200 mesh lacey carbon TEM grids with a Formvar support and glow discharged prior to use with a PELCO easiGlow Glow Discharge Cleaning System (Ted Pella, Inc.). Standard dissolution procedures were followed for sample preparation. After 60 min of incubation at 37 °C, each sample was centrifuged, and a 5 μL aliquot of the supernatant was applied to a TEM grid, held with tweezers within the Vitrobot chamber kept at 37 °C and 100% humidity (Figure S26). The sample was blotted once and plunged into liquid ethane for vitrification. After vitrification, each sample was stored in liquid nitrogen until imaging. Samples were imaged using the FEI Tecnai G2 F30 field emission gun transmission electron microscope, operated at an accelerating voltage of 300 kV, using a Gatan 626 cryo-holder, maintained at −175 °C. Images were digitally recorded using a Gatan UltraScan 4000 4k by 4k CCD camera.

X-ray Powder Diffraction (XRPD). After secondary drying, the ASD samples were analyzed using XRPD (Miniflex 600; Rigaku, Tokyo, Japan) to establish the presence or absence of crystallinity. The powder samples were packed in a zero-background silicon holder and exposed to Cu-K$_\alpha$ radiation (40 kV, 15 mA). Diffractograms were collected at RT in the reflection mode (Bragg−Brentano configuration) over a scattering angle of 2° ≤ 2θ ≤ 40° at a scanning rate of 5°/min with a 0.02° step size.

Scanning Electron Microscopy (SEM). The particle morphology of the ASD powders was examined using SEM. Sample preparation involved mounting the powders onto an aluminum stub with conductive carbon adhesive tabs (Ted Pella, Inc., Redding, CA), followed by sputter coating a 10 nm layer of iridium using an EMS/Quorum Q150T ES Plus (Electron Microscopy Sciences, Hatfield, PA). The sputtered samples were imaged with a Sigma 300 VP SEM (Carl Zeiss Microscopy, LLC, White Plains, NY) at an acceleration voltage of 1−2 kV and a working distance of ∼6 mm using an SE2 detector.

Table 1. Summary of Polymer Excipient Properties[e]

	composition[a] (VP/VA) (NIPAm/DMA)	M_n[b] (kDa)	M_w[b] (kDa)	$Đ$[b]	T_{cp}[c] (°C)	T_g[d] (°C)
HPMCAS-MF	n/a	40	80	2.00		121
PVPVA (Kollidon VA64)	64:36	20	40	2.00		108
BB-PVPVA-26-40-C$_2$H$_5$	73:27	120	170	1.36		137
PND-224-C$_{12}$H$_{25}$	66:34	25	26	1.06	44	142
PND-63-C$_{12}$H$_{25}$	66:34	7.2	7.4	1.02	61	130
BB-PND-62-36-COOH	67:33	230	270	1.16	44	139
BB-PND-62-36-PEG	67:33	240	290	1.22	39	128

[a]^{1}H NMR ratio of peak integrations: for VP/VA, 1H at 4.90−4.60 ppm to 1H at 4.26−3.87 ppm, and for NIPAm/DMA, 1H at 4.00 ppm to 6H at 2.90 ppm. [b]SEC-MALS in DMF with 0.05 M LiBr. [c]Cloud point measurements were determined at normalized transmittance ≤80%. [d]T_g determined by DSC at 3 °C/min in the second heating cycle as the temperature at the midpoint in the glass transition region. [e]Bottlebrush polymers are labeled as BB-composition-N_{sc}-N_{bb}-end-group, where N_{sc} is the side chain degree of polymerization and N_{bb} is the backbone degree of polymerization.

Scheme 1. Grafting-from Synthetic Scheme for BB-PVPVA[a]
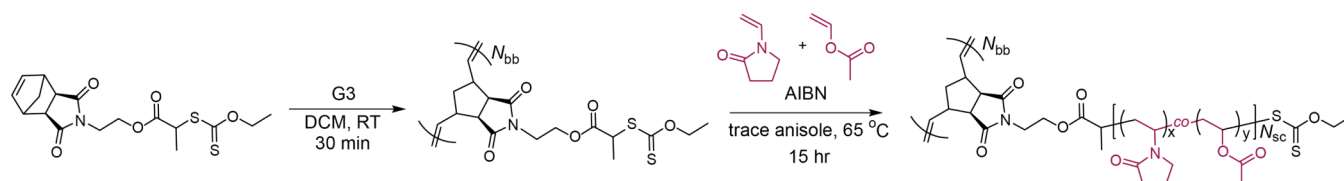
[a]First, a NB-XA CTA was ring-opened *via* ROMP with Grubb's 3rd generation catalyst (G3) at RT under an inert atmosphere. Then, MADIX polymerization was used to synthesize BB-PVPVA at 65 °C under bulk conditions with trace anisole. Further synthetic details are provided in Section S1.3.

Solid-State Nuclear Magnetic Resonance Spectroscopy (ssNMR). ssNMR experiments were performed on a Bruker Avance III spectrometer operating at a ^{1}H frequency of 500.13 MHz and a ^{13}C frequency of 125.77 MHz. Data were collected using a Bruker 4 mm HX standard bore solids probe (Bruker BioSpin, Billerica, MA). Samples were packed into 4 mm ZrO$_2$ rotors, sealed with Kel-F drive caps, and spun at the magic angle at 8000 ± 3 Hz. The sample temperature was controlled at 278 K. The dwell time was 13.3 ms, and 1024 data points were acquired for each free induction decay, which was zero-filled to 16,384 data points. Line broadening of 5 Hz was applied during processing. There were 256 or 512 data points used for each slice in relaxation time measurements. Ramped cross-polarization (CP) was applied for each experiment with a 70−100% ramp on the ^{1}H channel and a contact time of 1.5 ms.[44−46] The ^{1}H 90° pulse width was 2.9 μs, and the ^{1}H decoupling field strength was 86 kHz. Decoupling employed the SPINAL64 scheme with repeated 5.3 μs ^{1}H pulses.[47] Total sideband suppression (TOSS) was applied using a 5-p version of the experiment, with five ^{13}C 180° pulses of 7.2 ms each.[48,49] The pulse delay for 1D experiments was 2 s, and a total of 3888 scans were collected for each 1D spectrum displayed. The chemical shift regions unique to API and polymer peaks in the ASD spectrum were integrated to obtain proton relaxation times. ^{1}H T_1 relaxation times were measured *via* saturation recovery using a ^{13}C-detected CP pulse sequence with TOSS. Sixteen ^{1}H 90° pulses were employed to saturate ^{1}H magnetization, and 16 t delays varied from 0.05 to 10 s were used to measure saturation recovery and calculate T_1. A total of 32 or 64 scans were collected for each t slice. ^{1}H T_{1r} relaxation times were measured using a CP pulse sequence with an additional ^{1}H spin-locking period before CP. Sixteen ^{1}H spin-locking times varied from 0.05 to 50 ms were employed to measure T_{1r}, with 32, 64, or 128 scans collected for each slice.

Inductively Coupled Plasma Optical Emission Spectroscopy (ICP-OES). *Copper (Cu) and Ruthenium (Ru).* Copper and ruthenium content were determined in DMSO, with a combined calibration standard prepared. A four-point calibration curve was performed by diluting the 100 mg/L stock, ranging from 0.1 to 10 mg/L. System suitability passed by having an R^2 value > 0.99 and a RSD value of 1.0 mg/L sample <15. Solid samples were prepared by weighing approximately 45 mg into 15 mL tubes, then brought to ~9 mL. Samples were vortexed and then sonicated to ensure the polymer dissolved into solution. The instrument took 3 readings and provided an average for the final result.

Sulfur (S). Sulfur was run independently in an aqueous solution. Naturally, sulfur cannot be run in DMSO as there is sulfur intrinsically in the solvent. A 2% nitric acid solution was used to dissolve the solid sample into solution. A five-point calibration curve was performed by diluting the 100 mg/L stock, ranging from 1.0 to 50 mg/L. System suitability passed by having an R^2 value > 0.99 and a RSD value of 1.0 mg/L sample <15. Solid samples were prepared by weighing approximately 100 mg into 15 mL tubes, then brought to ~10 mL. Samples were vortexed and then sonicated to ensure the polymer dissolved into solution. The instrument took 3 readings and provided an average for the final result.

■ RESULTS AND DISCUSSION

Synthesis and Characterization of Excipient Library. Seven polymer excipients were used to explore the roles of polymer composition, architecture, molar mass, and surfactant concentration on dissolution efficacy and drug−polymer nanodroplet formation (Figure 1A). The wide range of formulations enabled comparisons between the structure−property relationships that dictate the performance of an excipient−drug pairing. Two linear PND copolymers and three bottlebrush polymer excipients were synthesized, as shown in

Figure 1B. Two of the polymer excipients are commercially available, HPMCAS-MF and PVPVA (Kollidon VA64). The commercial controls were used as benchmarks to compare with our designer excipients, as they have been studied and clinically utilized with a wide range of active pharmaceuticals. The controls have high dispersities ($Đ$ = 2.00) with weight average molecular weights of 80 and 40 kDa for HPMCAS-MF and PVPVA, respectively (Table 1). Commercial HPMCAS is industrially prepared by the functionalization of cellulose derivatives with two ethers, methoxy and hydroxypropyl, and two esters, acetate and succinate.[50] Commercial PVPVA derivatives are polymerized using free radical polymerization, leaving their architecture (linear *vs* branched) and sequence distribution (statistical or gradient) ill-defined.[51−53] Furthermore, it is difficult to control molecular weight with higher-order polymeric architectures (*e.g.*, bottlebrush polymers) using free radical polymerization.[52]

To understand the role of polymer architecture on PVPVA dissolution efficacy, we synthesized a PVPVA bottlebrush copolymer (BB-PVPVA) using grafting-from techniques (Scheme 1) with a norbornene-functionalized xanthate (NB-XA) chain transfer agent (CTA). A macro-CTA was synthesized from the NB-XA using ring-opening metathesis polymerization (ROMP), resulting in a XA-functionalized bottlebrush polymer backbone (N_{bb} = 40, M_w = 17 kDa, $Đ$ = 1.09). The PVPVA bottlebrush copolymer side chains were polymerized *from* the macro-CTA backbone *via* a reversible-deactivation radical polymerization (RDRP) technique called macromolecular design by the interchange of xanthate (MADIX). VA incorporates slowly into polymers in the presence of VP.[54] Despite 18 h reaction times, these polymerizations ran to low conversion (<50%). Therefore, front-loading the reaction with VA over VP ensured sufficient incorporation to mimic the commercial control, estimated to be a 64:36 molar ratio of VP/VA. The resulting bottlebrush polymer has an M_w of 170 kDa and a dispersity of 1.36 (Table 1).

Under the assumption that all the XA groups on the macro-CTA were activated and all polymer chains polymerized at the same rate, BB-PVPVA has 26 repeat units per side chain. The size exclusion chromatography traces of the BB-XA and BB-PVPVA in Figures S16 and S18 show the shift of the bottlebrush polymer to lower retention times, indicating an increase in molar mass. While others have synthesized a PVA-*graft*-PVP copolymer[55] or a bottlebrush polymer with PVP-*block*-PVA side chains,[56] this is the first time the copolymerization synthesis of a PVPVA bottlebrush copolymer has been reported to the best of our knowledge.

In addition to HPMCAS-MF and PVPVA-based excipients, PND excipients with a NIPAm/DMA molar ratio of 66:34, discovered through high-throughput screening of excipient formulations,[26] were also chosen for this study. PND-based excipients have shown utility in solubilizing highly crystalline APIs such as phenytoin. We examined the role of polymer molar mass *via* high and low molar mass linear PND variants (*i.e.*, PND-26k and PND-7k, respectively). We also examined the role of polymer architecture by selecting carboxylated and PEGylated PND bottlebrush excipients (*i.e.*, BB-PND-COOH and BB-PND-PEG), which were the first and second best performers, respectively, in solubilizing phenytoin in previous studies.[34] The syntheses of PND bottlebrushes with carboxylated or PEGylated end-groups (BB-PND-COOH and BB-PND-PEG) and high or low molar mass linear PND (PND-

26k and PND-7k) copolymer excipients were based on our previous publications and are described in Sections S1.1 and S1.2, respectively.[26,33,34,57] PND molecular weights and dispersities are provided in Table 1.

Each of the seven polymer excipients purchased or synthesized for this study was further characterized to define thermoresponsive properties and glass transition temperatures, as shown in Table 1. The cloud point temperature (T_{cp}) values for PNIPAm-containing polymers in this study are all above 37 °C, indicating adequate aqueous solubility, thus offering promising potential as oral drug carriers at this temperature (Section S2.7). Furthermore, due to the high glass transition temperatures of the polymer excipients in this study, we expect that the resulting ASD samples will have high shelf life stability at ambient or colder storage conditions (Section S2.8).

DLS was used to define the size of the polymer excipients in solution and their tendencies toward self-assembly or aggregation in the absence of the drug. The hydrodynamic radius (R_h) of each excipient measured at 3 mg/mL in FaSSIF-V2 and MB is summarized in Table 2. For reference, FaSSIF-

Table 2. Summary of Hydrodynamic Radii of Excipients Measured with DLS in MB or FaSSIF-V2 at 3 mg/mL[a]

sample	$R_{h, MB}$ (nm)	$R_{h, FaSSIF-V2}$ (nm)
FaSSIF-V2		16
HPMCAS-MF	11, 59	25
PVPVA	6.5	18
BB-PVPVA	15	25
PND-26k	11, 44	11, 34
PND-7k	8.3, 42	6.4
BB-PND-COOH	11	15
BB-PND-PEG	10	13

[a]Two values indicate bimodal or broad multimodal populations.

V2 in MB has a R_h of 16 nm due to the lecithin micelles dissolved in the solution. The HPMCAS-MF in MB was measured to exist as a multimodal population with two dominant populations with an average R_h of 11 and 59 nm. The larger population could indicate some cross-linking occurred during methylcellulose functionalization,[15] or polymer hydrophobicity is leading to an aggregated population. When HPMCAS-MF was analyzed in FaSSIF-V2, the HPMCAS-MF consolidated into a single population with a R_h of 25 nm (Figure S38B). This could be due to the ionic strength difference with the added bile salts or interactions with the lecithin in solution, promoting disassembly of the aggregated HPMCAS-MF population. The R_h values of the commercial PVPVA in MB and FaSSIF-V2 are 6.5 and 18 nm, respectively. The BB-PVPVA sample followed a similar trend to PVPVA, displaying increased size in FaSSIF-V2 (R_h = 25 nm) compared to MB (R_h = 15 nm).

Both the high- and low-molecular weight linear PND excipients formed micelles (R_h = 11 and 8.3 nm, respectively) in MB along with an aggregated population (Table 2). These linear copolymer excipients have been shown to form micelles due to hydrophobic self-assembly driven by the dodecyl hydrocarbon end-groups of the trithiocarbonate Z-group on the CTA.[30−33,57] For PND-26k in FaSSIF-V2, a broad size distribution exists with two dominant populations centered on R_h of 11 and 34 nm. In contrast, PND-7k exhibits a monomodal population with R_h = 6.4 nm in FaSSIF-V2, indicating that lecithin could break apart the aggregated
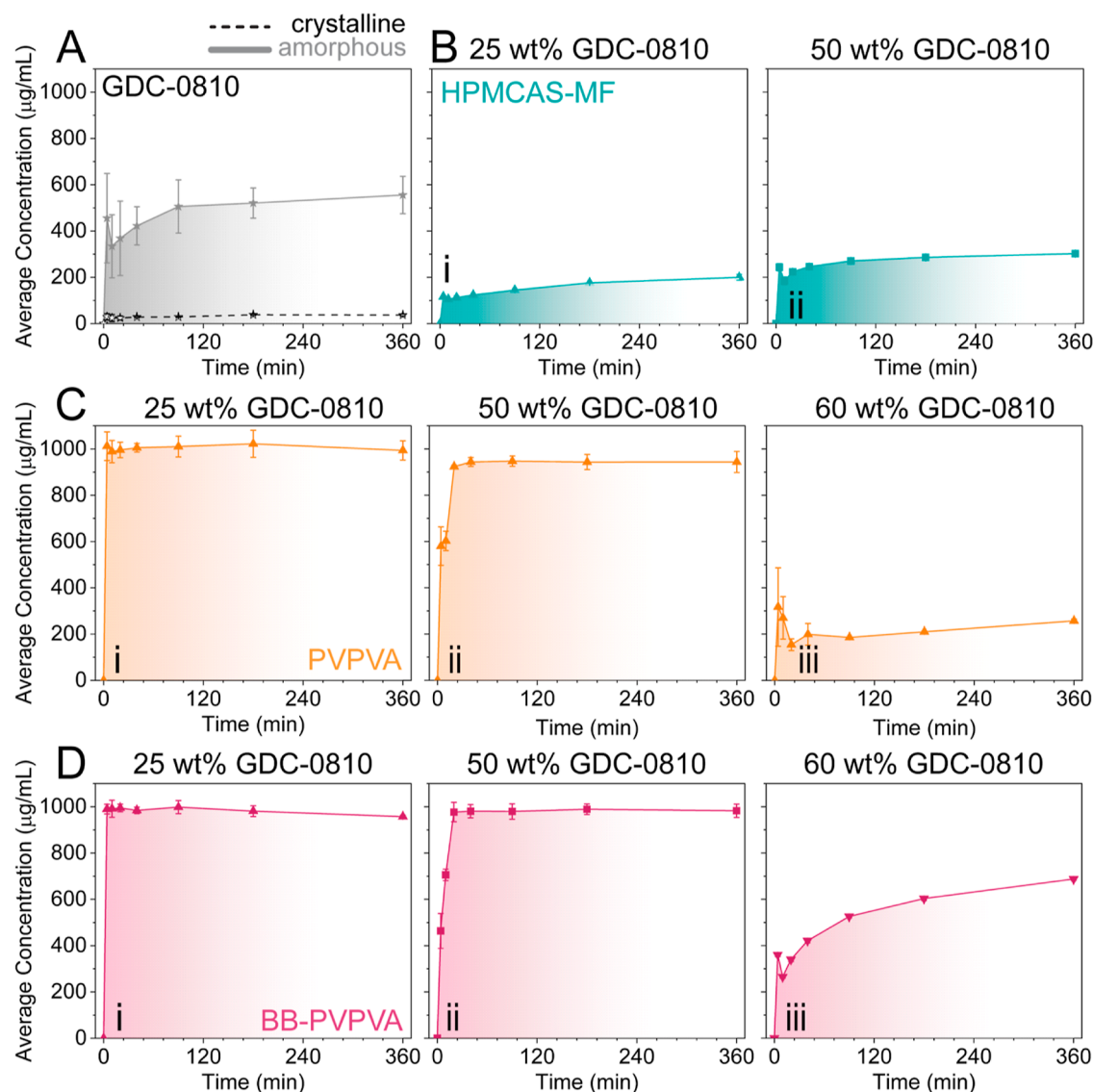
Figure 2. Dissolution performance of ASDs under non-sink conditions in 0.18 wt % FaSSIF-V2 with a pH 6.5 at 37 °C and a target GDC-0810 concentration of 1000 μg/mL. (A) Crystalline (dotted line) and amorphous (solid line) GDC-0810, (B) HPMCAS-MF at (i) 25 wt % and (ii) 50 wt % GDC-0810, (C) PVPVA at (i) 25 wt %, (ii) 50 wt %, and (iii) 60 wt % GDC-0810, and (D) BB-PVPVA with (i) 25 wt %, (ii) 50 wt %, and (iii) 60 wt % GDC-0810 loading.

population that was present in MB. The end-group-modified PND bottlebrush copolymers (BB-PND-COOH and BB-PND-PEG) each exist in solution as a monomodal population in both MB ($R_h \sim 11$ nm) and FaSSIF-V2, with R_h values slightly higher ($R_h \sim 14$ nm) in the FaSSIF-V2 solution (Table 2). This increase in size could be attributed to the averaging of joint scattering between the lecithin and copolymer in solution or the interaction of the copolymer excipients with the components of FaSSIF-V2. Overall, this data shows the unimolecular nature of the bottlebrush polymers in both MB and FaSSIF-V2 and the tendency toward self-assembly of both linear PND samples. This characterization of the polymer size in the absence of drug molecules will be important to understand how the nanostructures adapt to solubilize GDC-0810.

Spray-Dried Dispersion Formation and Dissolution. ASDs were prepared by spray-drying from a concentrated methanol solution, and each ASD was confirmed to be fully amorphous using PXRD (Figure S31), SEM (Figure S32), and

solid-state ^{13}C and ^{19}F NMR experiments (Figures S33 and S34). Sufficient mixing of polymer and drug within the ASD at nanometer length scales was determined by solid-state ^{1}H NMR $T_{1\rho}$ measurements (Table S3). ICP-OES analysis was conducted for PND-based ASDs at 25 wt % GDC-0810 to check for trace levels of toxic elements, and the data showed that PND formulations used in this study are within the federally allowed limit of elemental impurities for oral administration (Section S3.4).

We performed dissolution studies with GDC-0810 to compare the solubilization efficacy of the polymer excipients. The dissolution performance of each polymer excipient was tested and compared to the crystalline and amorphous solubility of GDC-0810 under non-sink dissolution conditions in 0.18 wt % FaSSIF-V2 with a pH of 6.5 at 37 °C at a target drug concentration of 1000 μg/mL (Figures 2 and 3). The purpose of using FaSSIF-V2 is to accurately model the contents and pH of the fasted state of the small intestine. At the concentrations within the 0.18 wt % FaSSIF-V2
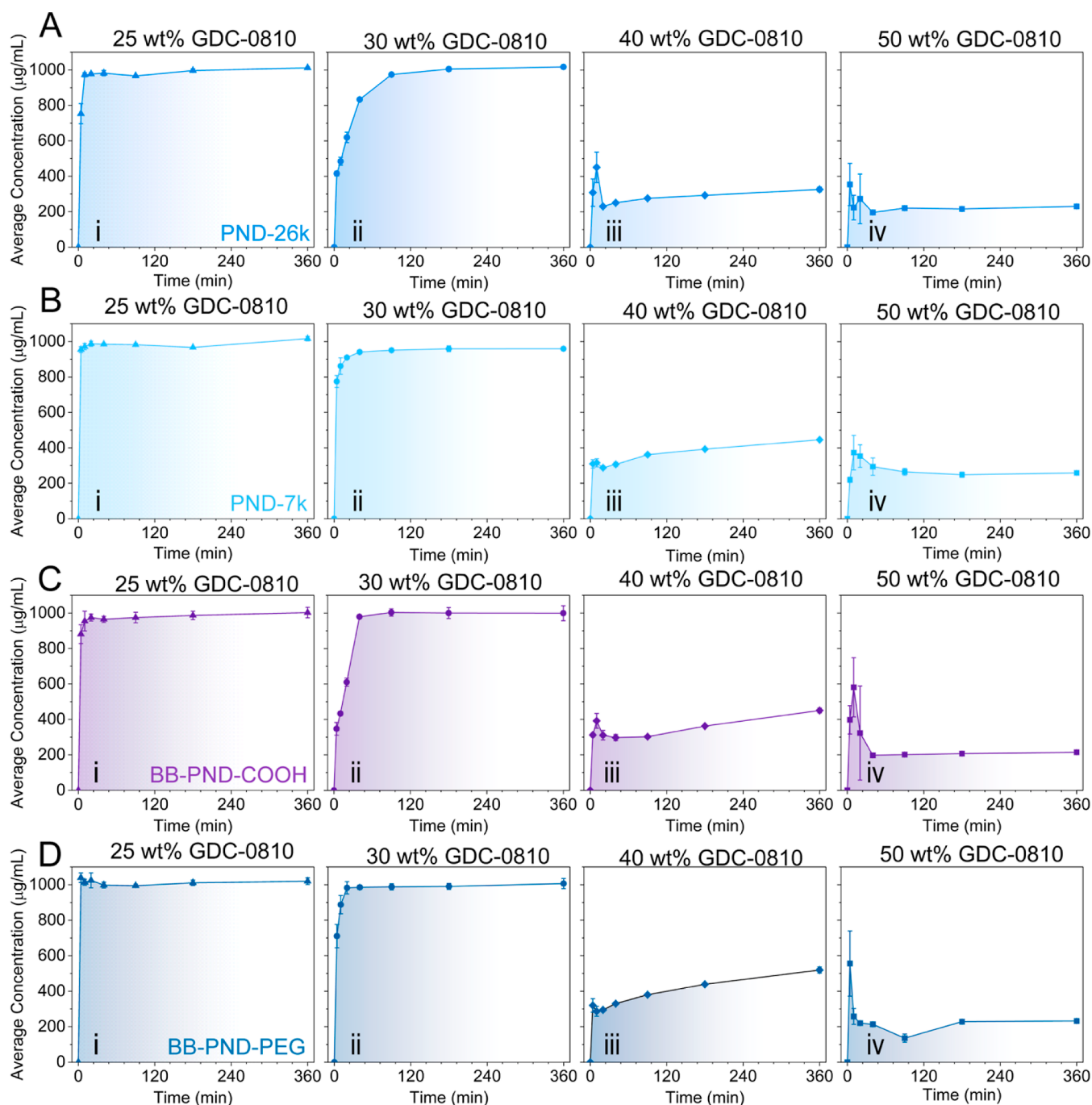
Figure 3. Dissolution performance of PND-based ASDs under non-sink conditions in 0.18 wt % FaSSIF-V2 at pH 6.5 and 37 °C with a target drug concentration of 1000 μg/mL with GDC-0810 concentrations of 25, 30, 40, and 50 wt % and the following polymer excipients: (A) PND-26k, (B) PND-7k, (C) BB-PND-COOH, and (D) BB-PND-PEG.

formulation (Table S1), lecithin is above its critical micelle concentration (CMC).[58,59] The micelle-forming ability of the phospholipid mixture that makes up lecithin in FaSSIF-V2 can act as a secondary equilibrium mechanism to improve the solubility of GDC-0810.[58] Dissolution studies in FaSSIF-V2 are designed to expose the synergistic effect of polymer and lecithin micelles in improving the solubility of GDC-0810 in a dissolution medium that more closely models the physiological state of the fasted small intestine.

Dissolution experiments under non-sink conditions were used to analyze the concentration of GDC-0810 over the course of 6 h *via* RP-HPLC. Figure 2A (dotted line) shows

that the crystalline solubility of GDC-0810 alone in FaSSIF-V2 is quite low (37 μg/mL). The amorphous solubility of GDC-0810 in FaSSIF-V2 is 560 μg/mL—a 15x increase over the crystalline solubility (Figure 2A, solid line). The drug alone exhibits good amorphous stability.[60] Therefore, it was surprising that the drug concentrations recorded for HPMCAS-MF ASDs loaded with 25 and 50 wt % GDC-0810 are below the amorphous solubility of GDC-0810 spanning the 6 h experiment [Figure 2B(i,ii)]. HPMCAS-MF has been shown to be an effective semisynthetic polymer for solubilizing a variety of commercially available ASDs.[61−65] Because GDC-0810 is a crystalline drug with T_m = 225 °C and
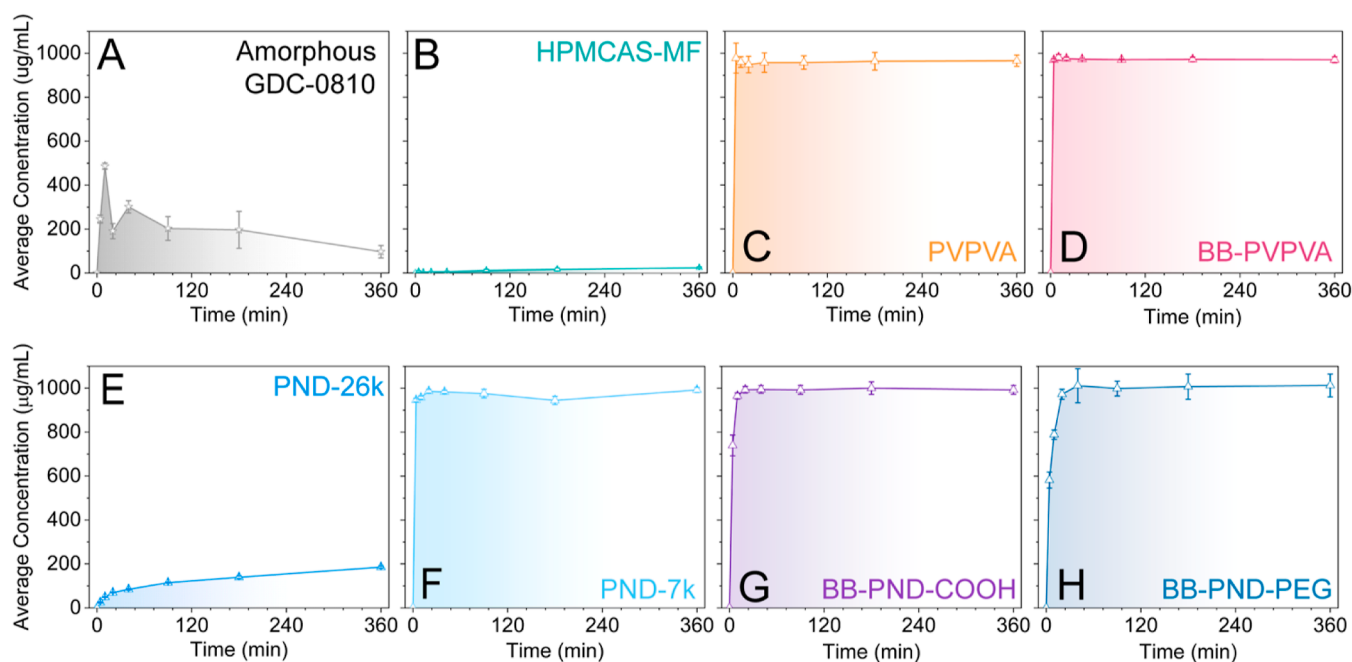
Figure 4. Dissolution results of GDC-0810 under non-sink conditions in MB at pH 6.5 and 37 °C with a target drug concentration of 1000 μg/mL. (A) Amorphous GDC-0810, (B) HPMCAS-MF at 25 wt % GDC-0810, (C) PVPVA at 25 wt % GDC-0810, (D) BB-PVPVA at 25 wt % GDC-0810, (E) PND-26k at 25 wt % GDC-0810, (F) PND-7k at 25 wt % GDC-0810, (G) BB-PND-COOH at 25 wt % GDC-0810, and (H) BB-PND-PEG at 25 wt % GDC-0810.

is relatively lipophilic with a log P of 6.2 (Figure S21B),[58] it is possible that the degree of methylcellulose functionalization with methoxy (~23 wt %), hydroxypropyl (~7 wt %), acetate (~9 wt %), and succinate (~12 wt %) moieties was not the correct balance needed to solubilize GDC-0810. At an intestinal pH of 6.5, HPMCAS is predominantly a colloidal suspension and is only sparingly soluble.[63] Indeed, Ricarte and co-workers showed that HPMCAS-MF had a negative second virial coefficient in phosphate-buffered saline at 37 °C, indicating a lack of adequate polymer−solvent interactions.[15] This could be responsible for the dissolution curve (Figure 2B), where HPMCAS-MF appeared to promote GDC-0810 insolubility. We speculate that HPMC or HPMCAS-LF may be a better excipient for GDC-0810 due to the 20% greater amount of unfunctionalized hydroxyl groups or lower acetyl/succinoyl ratio, respectively, that would aid with solubility enhancement of the ASD.

The commercial PVPVA and BB-PVPVA excipients were able to fully solubilize the targeted drug concentration of 1000 μg/mL of GDC-0810 at 25 through 50 wt % drug loading over the course of 6 h in FaSSIF-V2 at 37 °C, with the dissolution performance declining at 60 wt % drug loading (Figure 2C,D). Despite not achieving the full targeted drug concentration at 60 wt %, the BB-PVPVA formulation was able to solubilize 69% of the targeted drug concentration in comparison to the commercial control (PVPVA), which only solubilized 26% of the targeted concentration, a 167% increase in solubilized GDC-0810 compared to the commercial control. This confirms our hypothesis that polymer architecture influences GDC-0810 solubilization efficacy. Achieving GDC-0810 supersaturation at these high drug loadings for both commercial PVPVA and BB-PVPVA could be due to hydrogen bonding between the carbonyl groups in PVPVA and the secondary amine in the pyrazole ring in GDC-0810. Importantly, the synthesized BB-PVPVA significantly out-

performed the commercial control, HPMCAS-MF, at promoting solubilization of GDC-0810 at 25 wt % and above.

All the linear and bottlebrush PND copolymers were able to fully solubilize the targeted drug concentration of GDC-0810 at 25 wt % drug loading for 6 h [Figure 3A(i),B(i),C(i),D(i)] through 24 h (Figure S35) in FaSSIF-V2 at 37 °C. We propose that hydrogen bonding between the pyrazole ring of GDC-0810 and NIPAm moieties, in addition to hydrophobic interactions with n-clusters, is responsible for the super-saturation of GDC-0810 (see Section S4.3 for further discussion). At 30 wt % [Figure 3A(ii),B(ii),C(ii),D(ii)], each PND-based excipient was able to fully solubilize at the targeted 1000 μg/mL by 3 h. PND-7k and BB-PND-PEG displayed the shortest time to achieve the target concentration out of the four PND-based excipients at 30 wt % drug loading, indicating that the lower molecular weight and PEGylation helped increase initial dissolution rates, respectively. An expected decline in dissolution performance was observed at 40 wt % [Figure 3A(iii),B(iii),C(iii),D(iii)] and 50 wt % [Figure 3A(iv),B(iv),C(iv),D(iv)] for the PND-based excipients due to an oversaturation of NIPAm n-clusters with GDC-0810 molecules (see Sections S4.2 and S4.3).[27,28,34] Overall, these dissolution results in FaSSIF-V2 show that PND-based excipients are effective at maintaining super-saturation of GDC-0810 up to 30 wt %, whereas PVPVA-based excipients can maintain supersaturation up to 50 wt %, and the commercial control, HPMCAS-MF, fails to promote GDC-0810 supersaturation at 25 wt %, supporting our hypothesis that excipient composition affects GDC-0810 solubilization efficacy. To investigate if there is a synergistic effect between polymer excipients and surfactants in these formulations, we then evaluated polymer excipient performance in MB alone without FaSSIF-V2.

Role of FaSSIF-V2 on Dissolution Performance. Surfactants have been demonstrated to have a complex
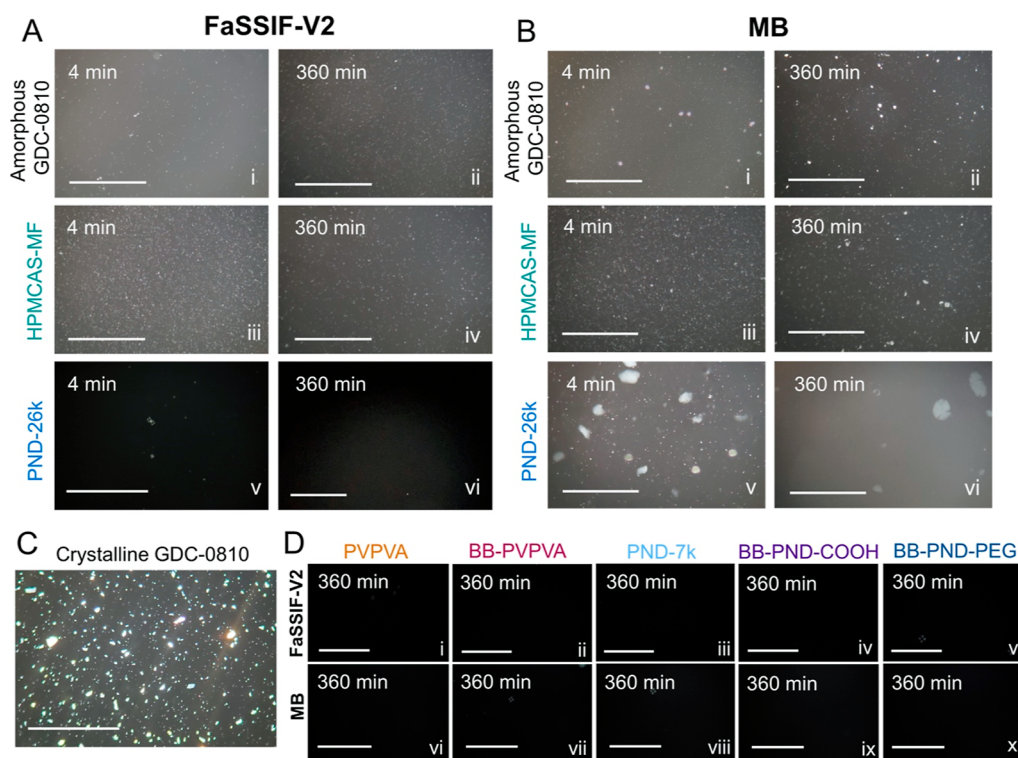
Figure 5. Representative polarized light microscopy micrographs of the dissolution samples after vortexing to suspend all insoluble material in solution. All ASDs contain 25 wt % GDC-0810. (A) Polarized light microscopy micrographs in FaSSIF-V2 at 4 and 360 min for amorphous GDC-0810 (i,ii), HPMCAS-MF (iii,iv), and PND-26k (v,vi). (B) Polarized light microscopy micrographs from dissolution experiments in MB at 4 and 360 min for amorphous GDC-0810 (i,ii), HPMCAS-MF (iii,iv), and PND-26k (v,vi). (C) Crystalline GDC-0810 in FaSSIF-V2. (D) Polarized light microscopy micrographs taken at 360 min in both FaSSIF-V2 and MB for PVPVA (i,vi), BB-PVPVA (ii,vii), PND-7k (iii,viii), BB-PND-COOH (iv,ix), and BB-PND-PEG (v,x). Scale bars = 500 μm.

influence on both crystallization inhibition and liquid–liquid phase-separation in ASDs.[66–68] Due to the micelle-forming ability of lecithin in FaSSIF-V2 and its ability to act as a secondary equilibrium mechanism to improve the solubility of GDC-0810, we isolated the effects of polymer excipient solubility enhancement of GDC-0810 by studying dissolution efficacy in MB alone (Figure 4). Upon removal of the 0.18 wt % FaSSIF-V2 from the MB, the amorphous GDC-0810 (Figure 4A) was found to have a more characteristic burst-like release profile with an initial solubility burst followed by a decrease in drug concentration over the course of 6 h, almost returning completely to the crystalline drug concentration. We speculate that the lecithin and bile salts included in the FaSSIF-V2 formulation facilitate the stabilization of liquid–liquid phase-separated amorphous drug droplets in solution (Figure 2A, solid line). Due to the destabilization of these droplets in the absence of FaSSIF-V2, all ASDs at 25 wt % drug loading were tested without FaSSIF-V2 present to decouple the excipient solubilization efficacy from the potential contributions of the surfactant and bile salts.

All ASD formulations promoted supersaturation of GDC-0810 at 25 wt % in MB, except for HPMCAS-MF and PND-26k. The average drug concentration achieved for 25 wt % GDC-0810 with HPMCAS-MF in MB (Figure 4B) was observed to be less than that of the crystalline drug concentration in FaSSIF-V2 (Figure 2A, dotted line). The HPMCAS-MF ASD with GDC-0810 is likely promoting drug insolubility in MB, as described earlier, due to polymer hydrophobicity. Despite fully solubilizing the targeted drug concentration in FaSSIF-V2, the solubilization performance of

the linear PND-26k with 25 wt % GDC-0810 significantly decreased in MB alone. We speculate that the presence of lecithin surfactants in the FaSSIF-V2 facilitates the breakup of large drug–polymer aggregates into the nanostructures necessary to effectively solubilize GDC-0810, as observed in Figure 3A(i) and discussed below in more detail. Importantly, the bottlebrush architectures, although higher in molecular weight than PND-26k, are better able to sequester and disperse hydrophobic amorphous drug droplets without extra surfactants present in the dissolution media due to the unimolecular drug-loaded nanoparticles that form in solution (Figures 6 and S38). This also confirms our hypothesis that polymer excipient molar mass influences dissolution performance, as evidenced by the differences between PND-7k and PND-26k without FaSSIF-V2.

Therefore, by comparing the dissolution data, we can conclude that without the extra surfactants in FaSSIF-V2, the PND-26k ASD is unable to effectively disperse in solution to achieve the targeted drug concentration, and the dissolution performance of the amorphous drug is significantly reduced. In addition, we can conclude that the performance of PVPVA-based, PND-7k, and PND-based bottlebrush excipients is less influenced by changing solution environments. Comparison between ASDs that were affected versus those unaffected by the absence of FaSSIF-V2 suggests that the drug–polymer nanoaggregate formation, size, and morphology are influencing GDC-0810 dissolution and sustained solubility with time. This was further explored using imaging techniques such as polarized light microscopy and cryogenic transmission electron microscopy, as well as DLS.
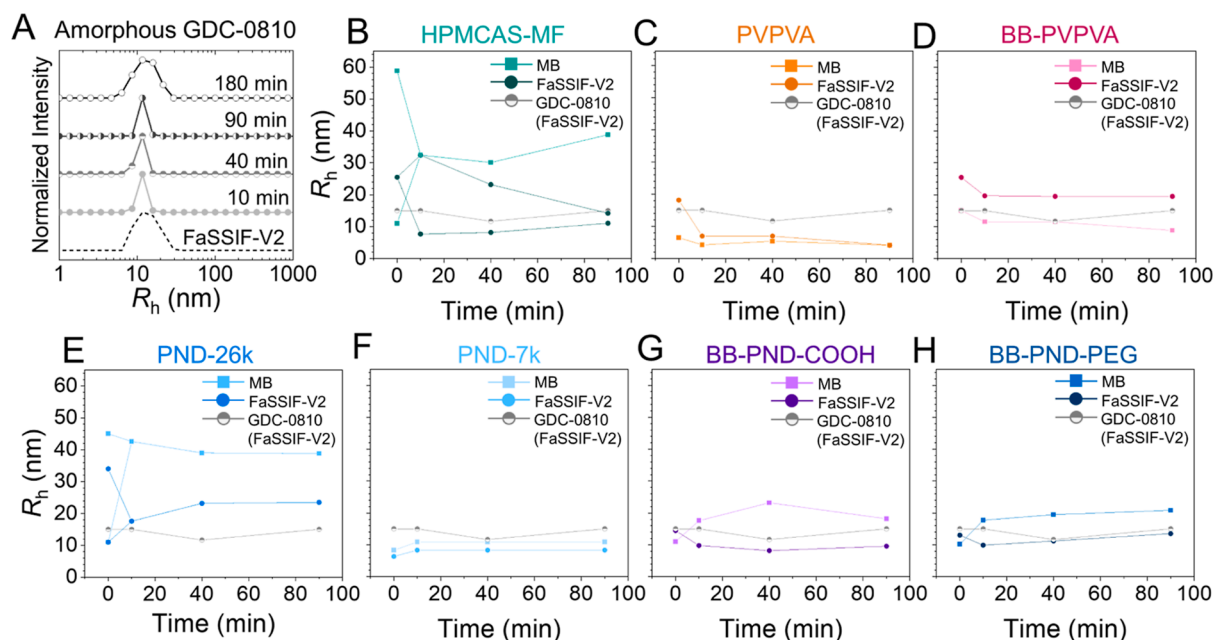
Figure 6. Hydrodynamic radius distributions as a function of time measured for drug−polymer nanoaggregates formed with 25 wt % GDC-0810 in MB (squares) and FaSSIF-V2 (circles) at 10, 40, and 90 min compared to (A) amorphous GDC-0810 in FaSSIF-V2, which is represented by the gray data lines in the hydrodynamic radius versus time plots for (B) HPMCAS-MF (multiple data points are indicative of a multimodal population observed by DLS), (C) PVPVA, (D) BB-PVPVA, (E) PND-26k (multiple data points are indicative of a multimodal population observed by DLS), (F) PND-7k, (G) BB-PND-COOH, and (H) BB-PND-PEG. Zero-minute time point corresponds to the polymer alone in solution at a concentration of 3 mg/mL. HPMCAS-MF and PND-26k exhibit multimodal distributions; therefore, there are two R_h data points plotted at those time points. For better visualization of these multimodal populations, all DLS traces exhibiting a distribution of sizes are shown in Figure S38.

Polarized Light Microscopy for Micron-Scale Characterization. Polarized light microscopy was used to examine the presence of birefringent or crystalline GDC-0810 particles over the course of the 6 h dissolution experiment in MB and FaSSIF-V2. In these studies, the ASD was visualized in solution after resuspension by vortexing, as opposed to sampling after centrifugation, to provide a holistic examination of the GDC-0810 and polymer excipient present in both the supernatant and pelleted ASD in cases of polymer−drug precipitation. ASD precipitation and subsequent drug recrystallization result from poor solubilization of the polymer excipient, drug, or both. Representative polarized light microscopy micrographs taken during dissolution are shown in Figure 5 and all micrographs are shown in Figures S39−S41; selected images of the precipitated pellet at 4 and 360 min are shown in Figure S42. The birefringent crystalline drug can be visualized, as shown in Figure 5C. In MB and FaSSIF-V2, polarized light microscopy revealed insoluble, anisotropic, amorphous GDC-0810 particles in solution. However, compared to the FaSSIF-V2 dissolution, in which the size of the birefringent precipitate remained constant [Figures 5A(i,ii) and S39B], the amorphous GDC-0810 in MB was visualized as a mixture of various sizes of insoluble, birefringent particles [Figures 5B(i,ii) and S40B], consistent with a burst-like amorphous dissolution behavior (Figure 4A). This is now attributable primarily to crystallization due to stability issues in the absence of a polymer excipient or surfactant.

In Figures 5A(iii,iv) and S40C, polarized light microscopy revealed that during the dissolution of HPMCAS-MF with 25 wt % GDC-0810 in FaSSIF-V2, many small crystalline particles were visible, some of which appear to be birefringent. For HPMCAS-MF with 25 wt % GDC-0810 in MB, polarized light microscopy showed many small crystalline particles with the occurrence of a few larger aggregated crystalline particles that may be birefringent at later time points [Figures 5B(iii,iv) and S41C]. The crystalline precipitate visualized in both FaSSIF-V2 and MB supports the notion that the HPMCAS-MF ASD is hydrophobic and not sufficiently interacting with the solvent.

In FaSSIF-V2, PND-26k fully solubilized the 1000 μg/mL of GDC-0810 from a 25 wt % drug-loaded ASD, as shown in Figure 3Ai and supported by the black polarized light microscopy images with no crystalline or birefringent particles in Figures 5A(v,vi) and S39F. This confirms observed dissolution trends (Figure 3A) that the PND-26k excipient is working synergistically with FaSSIF-V2 to maintain the supersaturation of GDC-0810. In contrast, in Figure 5B(v,vi), polarized light microscopy revealed small birefringent particles at the 4 min time point and large (∼150−250 μm) insoluble crystalline agglomerates of the PND-26k ASD in MB that persist throughout the 6 h dissolution experiment. There were no birefringent or crystalline particles present in the ASD systems with PVPVA, BB-PVPVA, PND-7k, BB-PND-COOH, or BB-PND-PEG as observed by the dark black images in both FaSSIF-V2 [Figures 5D(i−v) and S39] and MB [Figures 5D(vi−x) and S41], which agrees well with their rapid supersaturation of GDC-0810 at 25 wt %. Overall, these data support the dissolution results shown in Figures 2−4 and our hypothesis that the presence of surfactants in the dissolution media can mediate polymer−drug nanostructures and inhibit crystallization, thereby affecting the supersaturation of GDC-0810, particularly for the PND-26k excipient.

Dynamic Light Scattering for Nano-Scale Characterization. DLS was used to characterize the hydrodynamic radii of drug−polymer nanoaggregates formed within the FaSSIF-V2 or MB supernatant after centrifugation as a function of time over the course of the 6 h dissolution experiments. Each

sample was compared to the liquid–liquid phase-separated amorphous drug droplets (R_h = 11.7 nm) present during the dissolution of amorphous GDC-0810 in FaSSIF-V2 (Figure 6A, gray data points in Figure 6B–H). These results provide insight into why some excipients are more affected by the absence of FaSSIF-V2 than others. The zero-minute time point corresponds to the polymer alone in solution at a concentration of 3 mg/mL (summarized in Table 2). For HPMCAS-MF with 25 wt % GDC-0810 in FaSSIF-V2, the population in solution is multimodal, with a smaller population around 10 nm in R_h and a larger population starting above 30 nm in R_h that decreases in size over time (Figure 6B). In MB, for the HPMCAS-MF ASD particles that remain in solution after centrifugation and filtration, the particle size is an aggregated population with R_h greater than 30 nm, which were observed to be crystalline and insoluble by polarized light microscopy and dissolution studies. In contrast, the commercial PVPVA ASD was observed to form extremely small drug–polymer nanoparticles in both FaSSIF-V2 and MB, 4–7 nm in R_h, decreasing in size from the polymer alone with an R_h of 18 nm in FaSSIF-V2 and 6.5 nm in MB, suggesting strong polymer–drug noncovalent binding and compaction of the nanoparticles (Figure 6C), resulting in a lower size for the ASD than the polymer alone. The BB-PVPVA excipient forms nanostructures with GDC-0810 during dissolution (R_h = 20 nm in FaSSIF-V2 and 12 nm in MB) that are double the size of the commercial PVPVA ASD. However, the drug–polymer nanostructure measured during dissolution is smaller in R_h than the polymer alone in solution, suggesting similar compaction of the drug within the unimolecular nanoparticle as observed with the commercial PVPVA.

The PND-26k without drug (Table 2) at 3 mg/mL in MB exists as a bimodal population of self-assembled micelles driven by the hydrophobic associations of the dodecyl hydrocarbon tail and an aggregated population that is similar in size to that of nanoparticles formed with drug (Figure 6E). The aggregated population becomes the only population remaining in the supernatant during dissolution with 25 wt % GDC-0810 with an average R_h of 40 nm (Figure 6E). These larger nanoaggregates correspond to the formulation's inability to solubilize the polymer–drug without FaSSIF-V2 as observed *via* dissolution (Figure 4E) and the large, anisotropic agglomerates present in solution visualized by polarized light microscopy [Figure 5B(v,vi)]. With the help of lecithin surfactants present in FaSSIF-V2, the large drug–polymer nanoaggregates break up quickly and exist as a monomodal population with an R_h equal to 24 nm (Figure 6E). The low molecular weight PND-7k solubilizes GDC-0810 in both MB and FaSSIF-V2 as nanoparticles with R_h of 11 and 8 nm, respectively (Figure 6F), which are both smaller than the liquid–liquid phase-separated amorphous GDC-0810 droplets. Stable drug–polymer nanoparticle formation was expected and observed to occur rapidly for the low molecular weight PND-7k excipient due to its surfactant-like nature, leading to tolerance in differing dissolution media.

As observed previously, the PND-based bottlebrush copolymer excipients, BB-PND-COOH and BB-PND-PEG, exist in MB as unimolecular particles that are around 11 nm in R_h (Table 2). Upon dissolution with 25 wt % GDC-0810 in MB, the bottlebrush excipients become loaded with drug and increase in R_h to 23 and 19 nm at 40 min, respectively (Figure 6G,H). In FaSSIF-V2, the polymer–drug nanoparticles decrease in size to below or equal to the size of the liquid–
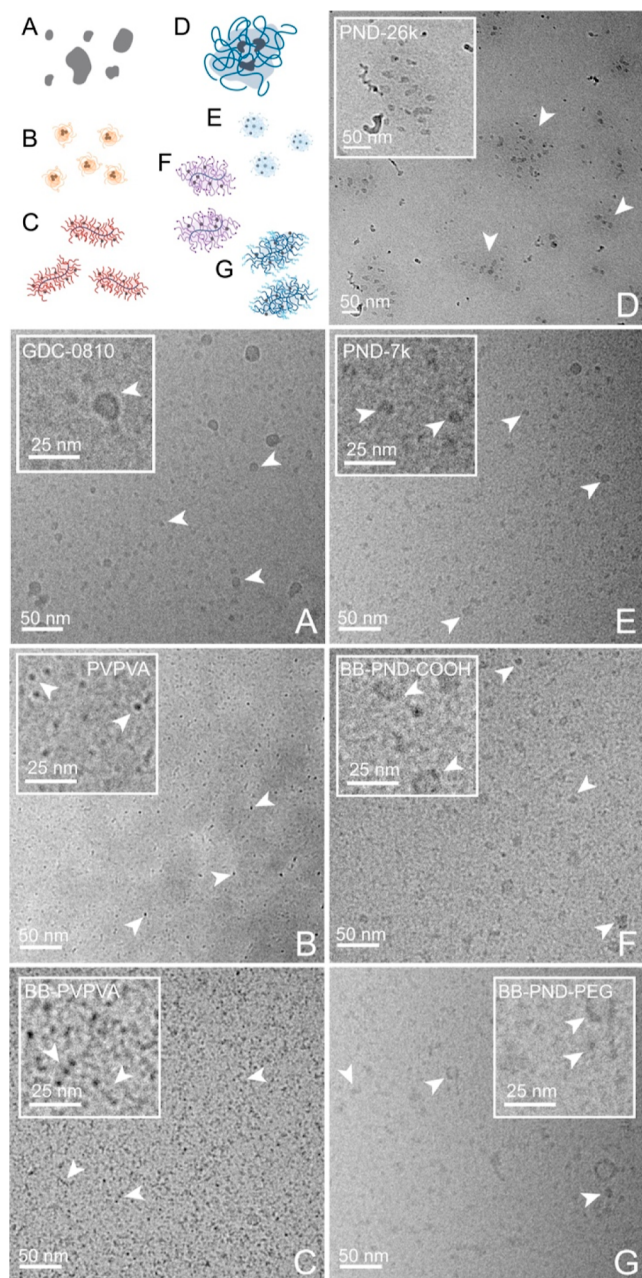
liquid phase-separated amorphous GDC-0810 droplets during dissolution for BB-PND-COOH and BB-PND-PEG, respectively. The PND bottlebrushes are the only samples for which R_h values increased in FaSSIF-V2 compared to MB for polymer-only samples but decreased in FaSSIF-V2 compared to MB for the corresponding ASDs. The increase in R_h for polymer-only samples is attributed to an averaging of joint scattering from the lecithin and polymer populations. Therefore, the decrease in R_h with drug present could indicate the lecithin micelles in FaSSIF-V2 cooperatively solubilized some of the GDC-0810, which reduced drug-loaded bottlebrush polymer size in FaSSIF-V2.

All the polymer excipients in this study, aside from PND-26k in MB and HPMCAS-MF, form drug–polymer nanoaggregates during dissolution in FaSSIF-V2 solution with $R_h \leq 25$ nm. Additionally, PVPVA and PND-7k ASD samples were observed to have generally unchanged drug–polymer nano-aggregate size during dissolution in both MB and FaSSIF-V2 (Figure 6C,F) and nanoparticle sizes less than that of the liquid–liquid phase-separated amorphous GDC-0810 droplets. The PVPVA and PND-7k ASD samples also achieve the target GDC-0810 concentration in MB (Figure 4) and FaSSIF-V2 (Figures 2 and 3) faster than the other excipients in the library, indicating that maintaining consistent nanoparticle sizes across the dissolution experiment below the liquid–liquid phase-separated amorphous drug droplet size is conducive to rapid supersaturation achievement. Overall, we deduce a general trend from Figure 6 that defines a successful excipient to be one that forms a drug–polymer nanoparticle in solution that does not exceed a R_h of 25 nm.

Cryogenic Transmission Electron Microscopy for the Visualization of Nanostructures. Cryo-TEM was used to visualize the nanostructures that produced the top performing ASD systems. The electron density afforded by the chlorine and fluorine functional groups on the GDC-0810 molecule facilitates visualization of the drug–polymer nanoaggregate structures without the need for secondary contrast agents. Cryo-TEM samples were prepared from the supernatant after centrifugation of the 25 wt % GDC-0810 ASDs at 60 min during dissolution. For the amorphous GDC-0810 in FaSSIF-V2, we observed dark, generally spherical, droplets of amorphous GDC-0810 that evidence liquid–liquid phase-separation in solution, stabilized by the lecithin micelles in the FaSSIF-V2 formulation (Figures 7A and S43). These liquid–liquid phase-separated nanodroplets of drug correspond to the size of particles that were observed during dissolution by DLS, R_h = 11.7 nm (Figure 6A).

Based on the cryo-TEM images in Figures 7B and S44, the PVPVA ASD appears to be present as many high-contrast, small, and isolated nanoparticles. This is supported by the formation of small drug–polymer nanoparticles with a R_h of 4–7 nm documented by DLS (Figure 6C) as well as the rapid supersaturation of GDC-0810 during dissolution in FaSSIF-V2 (Figure 2C). For the BB-PVPVA sample (Figures 7C and S45), we observed high contrast dots in the cryo-TEM micrograph like the commercial PVPVA, but these high contrast regions appear more tightly packed together and interconnected in comparison to the structures in Figure 7B. This suggests the side chains of the PVPVA bottlebrush are compacting the drug into rod-like structures along the polynorbornene backbone.

We postulate that if this behavior is maintained at higher GDC-0810 drug loadings in FaSSIF-V2, this interconnected
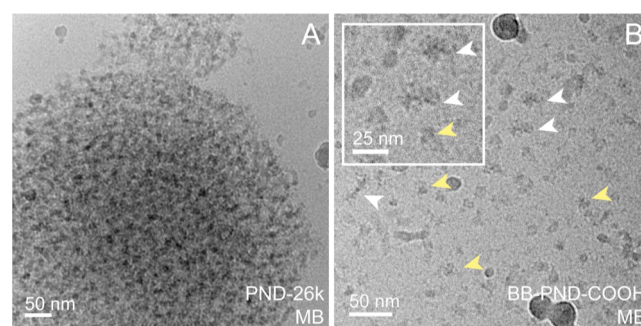
Figure 7. Cryo-TEM images of aliquots taken at 60 min during dissolution with 25 wt % drug-loading with each excipient in FaSSIF-V2 at pH = 6.5 and 37 °C. (A) amorphous GDC-0810, (B) PVPVA, (C) BB-PVPVA, (D) PND-26k, (E) PND-7k, (F) BB-PND-COOH, and (G) BB-PND-PEG.

observed in Figure 7C because there is less polymer material per drug, so there must be more GDC-0810 molecules per nanodroplet.

The PND-26k drug−polymer nanoarchitectures in FaSSIF-V2 at 60 min were visualized as amorphous drug droplets, around 10 nm in radius−similar to the size of the amorphous GDC-0810 in Figure 7A−but these drug nanodroplets are surrounded by a lower contrast cloud of what we believe to be polymer excipient (Figures 7D and S47). Since the targeted drug concentration was reached within 10 min with FaSSIF-V2 present in the dissolution media (Figure 3A), we believe that the surfactants in FaSSIF-V2 aid the distribution, solubility, and initial dissolution of the liquid−liquid phase-separated drug droplets within the hydrophobic drug-laden ASD, resulting in these more diffuse nanostructures. For PND-7k, which was observed to form much smaller particles (around 8 nm in R_h during dissolution as measured by DLS, Figure 6F), we visualized small, circular, and low contrast particles of approximately 10 nm in diameter *via* cryo-TEM (Figures 7E and S46). This suggests the drug is being concentrated in the middle of the micelle-like nanoparticles and surrounded by polymers. A similar phenomenon was reported with linear PND and phenytoin.[16] Therefore, the molecular weight of the linear PND copolymer excipient significantly influences the nanoaggregate morphology during dissolution. Lastly, for the BB-PND-COOH and BB-PND-PEG ASDs, cryo-TEM revealed discrete drug-loaded nanoparticles during dissolution with 25 wt % GDC-0810 in FaSSIF-V2 (Figures 7F,G, S49, and S51). The PND bottlebrush-based ASD particles visualized in FaSSIF-V2 are droplet-like and more oblong in shape than the PND-7k spherical nanoparticles (Figure 7E). Collectively, these results show that PND-26k solubilizes GDC-0810 as large islands whose solubility is facilitated by the surfactants in FaSSIF-V2, the PND-7k ASD forms much smaller particles with the drug concentrated in the center of the micelle-like nanoparticles, and the PND bottlebrush ASDs exist as droplet-like nanoparticles consistent with the bottlebrush architecture.

Two representative samples were imaged with cryo-TEM in MB during dissolution to compare a system that is dependent on FaSSIF-V2 for drug−polymer solubilization, PND-26k, and BB-PND-COOH, which is independent of the solution conditions. Figure 8A shows the dissolution supernatant at 60 min when sampled after centrifugation and visualized using cryo-TEM. Through these images, we gained further insight into how the PND-26k ASD is forming large drug−polymer

structure could be responsible for the BB-PVPVA outperforming PVPVA at 60 wt % (Figure 2). The critical overlap concentration (*c**) values for the polymers in Figure 7 were calculated using radius of gyration (*R*_g) values from the literature[34] or persistence length values.[69−73] The polymer concentrations during dissolution are 1−2 orders of magnitude below their *c** for all drug loadings tested. We assume the nanodroplet size is relatively constant at different drug loadings within this dilute regime (*c* ≪ *c**) as it is driven by polymer properties (*i.e.*, R_h values for ASDs in Figure 6 are close to those of polymers without drugs in Table 2). Therefore, we can reasonably predict an even higher degree of GDC-0810 compaction for BB-PVPVA at higher drug loading than that

Figure 8. Cryo-TEM images of (A) PND-26k and (B) BB-PND-COOH (white arrows = side view of bottlebrush and yellow arrows = end-on view of bottlebrush) with 25 wt % GDC-0810 at 60 min during dissolution in MB (pH = 6.5) at 37 °C. Scale bar = 50 nm.

aggregates, greater than 600 nm in diameter, which were observed at different stages of particle breakup (Figures 8A and S48); this behavior was not recorded by DLS due to the 0.2 μm cutoff in the filter used to prepare the specimens. For reference, the aggregates observed for PND-26k ASD in MB *via* polarized light microscopy were 150−250 μm in diameter [Figure 5B(v,vi)]. This confirms that without the synergistic solubilization with the lecithin micelles from FaSSIF-V2, the PND-26k ASD with 25 wt % GDC-0810 was hydrophobic, which prevented ASD dissolution.

Contrastingly, for BB-PND-COOH ASD with 25 wt % GDC-0810, cryo-TEM revealed discrete drug-loaded nano-particles in MB (Figures 8B and S50), which was consistent with the formulation's dissolution performance (Figure 4G). Compared to the droplet-like nanostructures in FaSSIF-V2 (Figure 7F), larger and more diffuse nanoparticles were observed in MB, where the side chains emanating from the polymer backbone could be visualized (inset of Figure 8B), corresponding to the increase in size, as shown in Figure 6G. The elliptical shape of the bottlebrush architecture was evidenced by the side view (white arrows) and end-on view (yellow arrows) projections of the bottlebrushes in Figure 8B. The distribution of contrast in these images allowed us to formulate a mechanism by which BB-PND-COOH solubilizes GDC-0810 without the presence of lecithin in the FaSSIF-V2. Higher contrast dots can be seen along the backbone and near the ends of the bottlebrush side chains, with less intense contrast along the side chains extending from the polymer backbones. This suggests compaction of GDC-0810 within the backbone as well as polymer−drug hydrogen bonding interactions with the carboxylated end-groups. In previous studies, the importance of hydrophilic bottlebrush end-groups was demonstrated with the small molecule phenytoin,[34] but this work shows that there could be noncovalent interactions with the end-groups as visualized by the chain end-proximity to the darker contrast drug regions using cryo-TEM. The separation of the higher contrast drug-loaded elliptical bottlebrushes visualized in MB supports the expectation that PND bottlebrush copolymer excipients solubilize APIs as unimolecular nanoparticles.

Excipient Design Considerations. Considering a holistic examination of the results above regarding the influence of polymer excipient composition, architecture, molar mass, and the presence of surfactants on ASD dissolution efficacy and drug−polymer nanodroplet formation with GDC-0810, we can define intersectional conclusions that will aid in the formulation of excipient−drug pairing rules. First, we identified that PVPVA-based excipients outperformed PND-based and HPMCAS excipients at effectively promoting the super-saturation of GDC-0810 at drug loadings of 50+ wt % (Figure 2C,D) due to the formation of small, compacted drug-rich nanodroplets that were observed *via* DLS and cryo-TEM measurements at 25 wt % GDC-0810 (Figures 6C,D and 7B,C). These uniquely compact drug−polymer nanostructures, which we believe are facilitated by hydrogen bonding between the polymer and drug, help facilitate the solubility of GDC-0810 at high drug loadings of 50 wt % and above. It is evident that the morphology of nanostructures formed between polymer and drug can be used to predict excipient efficacy as the morphology of the PND-based polymer drug nanostructures is vastly different than that of PVPVA-based samples.

Second, we highlighted the importance of drug−polymer nanodroplet formation leading to the rapid dissolution of GDC-0810. This was demonstrated best by the variation of nanostructures observed across the four PND derivatives used in this study. Previous work with low molecular weight PND and the BCS Class II API, phenytoin, indicated that lower molecular weight PND noncovalently binds the drug more strongly due to increased coronal density in the self-assembled micelle.[33] The contrast between the solubilization mechanisms of PND-26k and PND-7k indicates that the tighter binding due to the surfactant-like quality of PND-7k facilitates the formation of abundant discrete nanoparticles (Figure 7E), encouraging stronger polymer−drug interactions. This con-trasts with the large islands of amorphous drug droplets surrounded by the higher molecular weight PND-26k, where the drug and polymer exist with a higher degree of separation in solution (Figure 7D). These large islands of polymer surrounding several amorphous drug droplets, presumably associated with liquid−liquid phase-separation, are consistent with the drug solubilization mechanisms for PND investigated previously.[16] The cryo-TEM images for BB-PND-COOH and BB-PND-PEG confirm that bottlebrush excipients are solubilizing APIs as discrete unimolecular drug-loaded nano-particles (Figure 7F,G). The synthetically forced association between the PND side chains along the bottlebrush backbone and the self-assembled surfactant-like qualities of PND-7k excipients have been shown to drive polymer−drug inter-actions, resulting in stronger noncovalent binding between the polymer and API.[30−32] Therefore, the PND-based bottlebrush architectures and PND-7k excipients are better able to sequester and disperse hydrophobic amorphous drug droplets without relying on surfactants in the dissolution media.

Future *in vivo* studies will be necessary to investigate how the morphology of polymer−drug nanodroplets impacts API permeability and pharmacokinetics. Although outside the scope of this work, comparing the bioavailability of amorphous drug droplets stabilized by the diffuse island-like PND-26k to the compacted polymer−drug nanoparticles formed by the PVPVA-based excipients will be important to designing future API-excipient pairings. We predict the design rules for nanodroplet size and morphology observed in our studies to hold true for other BCS Class II small molecule APIs with a similar log P and T_m to that of GDC-0810. Overall, this data shows that polymer composition, architecture, molar mass, and surfactant concentration all impact the nanoparticle morphol-ogy of GDC-0810 ASDs, which we propose is responsible for dissolution behavior, *e.g.*, PVPVA-based excipients outperform-ing PND-based excipients at higher drug loadings.

◼ CONCLUSIONS

In conclusion, we compared a library of seven copolymer excipients that were spray-dried with GDC-0810 to form amorphous solid dispersions. Each of the excipents, HPMCAS-MF, PVPVA, BB-PVPVA, PND-26k, PND-7k, BB-PND-COOH, and BB-PND-PEG was investigated to compare the roles of excipient composition, architecture, molar mass, and sensitivity to surfactants in dissolution media (FaSSIF-V2 *vs* MB) on drug−polymer nanodroplet formation and solubility enhancement in aqueous solution. HPMCAS-MF was found to be an ineffective excipient for GDC-0810 due to polymer hydrophobicity, leading to few polymer−solvent interactions and devitrification of the drug during dissolution. PVPVA, a commonly used copolymer excipient in ASD formulations, was

incorporated into a bottlebrush polymer architecture for the first time *via* MADIX copolymerization in this study. Both PVPVA-based excipients, commercial and bottlebrush, offer exceptional drug-loading capacity for GDC-0810 and are thought to be hydrogen bonding with GDC-0810, leading to strong polymer−drug interactions, resulting in compacted drug−polymer nanoaggregates in solution visualized with cryo-TEM. These compact nanostructures could be contributing to the successful solubilization of GDC-0810 at high drug loadings of 50 wt % and above. In the case of the BB-PVPVA excipient, the formation of nanostructures with GDC-0810 compacted along the polymer backbone was shown to increase the drug-loading capacity, with the remarkable top formulation solubilizing 69% of the targeted drug concentration (688 μg/mL) from a 60 wt % GDC-0810-loaded ASD. The PND-based excipients are proposed to interact with the drug through hydrogen bonding and hydrophobic interactions. In addition, PND-based excipients that are surfactant-like (PND-7k) or bottlebrush architectures are less sensitive to the presence or absence of lecithin surfactants and solubilize GDC-0810 either as micelle-like drug−polymer nanoparticles or drug-loaded unimolecular nanoparticles. In comparison, PND-26k, together with lecithin surfactants, solubilized GDC-0810 in FaSSIF-V2 by stabilizing the liquid−liquid phase-separated amorphous drug droplets within a diffuse polymer−drug island. In summary, we conclude that a broad range of synthesized polymer excipients are suitable for solubilizing GDC-0810 and outperform the commercial control, HPMCAS-MF. Overall, we define an effective excipient as one that forms a drug−polymer nanoaggregate in solution with a hydrodynamic radius up to 25 nm with a tightly compacted nanodroplet morphology, idealized by the BB-PVPVA ASD. Drug−polymer nanodroplet formation and morphology during dissolution is a key factor in defining successful excipient drug pairings, aiding in the design and prediction of new excipients for challenging pipeline drug candidates.

■ ASSOCIATED CONTENT

Ⓢ Supporting Information

The Supporting Information is available free of charge at https://pubs.acs.org/doi/10.1021/acs.bioconjchem.4c00018.

General information, polymer synthetic procedures, ^{1}H and ^{13}C NMR spectroscopy, SEC-MALS, transmittance measurements, DSC thermograms, ASD solid-state characterization, ICP-OES discussion, dissolution results, discussion of PND n-clusters and noncovalent interactions, DLS distributions, polarized light microscopy images, and cryogenic transmission electron microscopy images (PDF)

■ AUTHOR INFORMATION

Corresponding Authors

Frank S. Bates − *Department of Chemical Engineering and Materials Science, University of Minnesota, Minneapolis, Minnesota 55455, United States;* ⓞ orcid.org/0000-0003-3977-1278; Email: bates001@umn.edu

Theresa M. Reineke − *Department of Chemistry, University of Minnesota, Minneapolis, Minnesota 55455, United States;* ⓞ orcid.org/0000-0001-7020-3450; Email: treineke@umn.edu

Authors

Kaylee E. Barr − *Department of Chemical Engineering and Materials Science, University of Minnesota, Minneapolis, Minnesota 55455, United States;* ⓞ orcid.org/0000-0002-2304-8205

Monica L. Ohnsorg − *Department of Chemistry, University of Minnesota, Minneapolis, Minnesota 55455, United States;* Present Address: Department of Chemical and Biological Engineering, University of Colorado Boulder, Boulder, CO 80309, United States; ⓞ orcid.org/0000-0002-7616-3880

Lucy Liberman − *Department of Chemical Engineering and Materials Science, University of Minnesota, Minneapolis, Minnesota 55455, United States; Department of Chemistry, University of Minnesota, Minneapolis, Minnesota 55455, United States;* Present Address: Wolfson Department of Chemical Engineering, Technion—Israel Institute of Technology, Haifa, Israel.; ⓞ orcid.org/0000-0001-9139-1163

Louis G. Corcoran − *Department of Chemistry, University of Minnesota, Minneapolis, Minnesota 55455, United States;* ⓞ orcid.org/0000-0003-3061-8808

Apoorva Sarode − *Synthetic Molecule Pharmaceutical Sciences, Genentech, Inc., South San Francisco, California 94080, United States;* ⓞ orcid.org/0000-0003-4096-7534

Karthik Nagapudi − *Synthetic Molecule Pharmaceutical Sciences, Genentech, Inc., South San Francisco, California 94080, United States*

Christina R. Feder − *Synthetic Molecule Pharmaceutical Sciences, Genentech, Inc., South San Francisco, California 94080, United States*

Complete contact information is available at:
https://pubs.acs.org/10.1021/acs.bioconjchem.4c00018

Author Contributions

□K.E.B. and M.L.O. contributed equally. This manuscript was written through the contributions of all authors. All authors have given their approval to the final version of the manuscript.

Notes

The authors declare no competing financial interest.

■ ACKNOWLEDGMENTS

polarized light microscopy data. The TOC, Figure 1A, and nanostructure illustrations in Figure 7 were made by the authors on Biorender.com.

■ REFERENCES

(1) Baghel, S.; Cathcart, H.; O'Reilly, N. J. Polymeric Amorphous Solid Dispersions: A Review of Amorphization, Crystallization, Stabilization, Solid-State Characterization, and Aqueous Solubilization of Biopharmaceutical Classification System Class II Drugs. *J. Pharm. Sci.* **2016**, *105* (9), 2527−2544.

(2) Wen, H.; Park, K. *Oral Controlled Release Formulation Design and Drug Delivery: Theory to Practice*; John Wiley and Sons, Inc., 2010.

(3) Yu, D.; Li, J.; Wang, H.; Pan, H.; Li, T.; Bu, T.; Zhou, W.; Zhang, X. Role of Polymers in the Physical and Chemical Stability of Amorphous Solid Dispersion: A Case Study of Carbamazepine. *Eur. J. Pharm. Sci.* **2022**, *169*, 106086.

(4) Ting, J. M.; Porter, W. W.; Mecca, J. M.; Bates, F. S.; Reineke, T. M. Advances in Polymer Design for Enhancing Oral Drug Solubility and Delivery. *Bioconjugate Chem.* **2018**, *29* (4), 939−952.

(5) Bhujbal, S. V.; Mitra, B.; Jain, U.; Gong, Y.; Agrawal, A.; Karki, S.; Taylor, L. S.; Kumar, S.; Tony Zhou, Q. Pharmaceutical Amorphous Solid Dispersion: A Review of Manufacturing Strategies. *Acta Pharm. Sin. B* **2021**, *11* (8), 2505−2536.

(6) Williams, H. D.; Trevaskis, N. L.; Charman, S. A.; Shanker, R. M.; Charman, W. N.; Pouton, C. W.; Porter, C. J. H. Strategies to Address Low Drug Solubility in Discovery and Development. *Pharmacol. Rev.* **2013**, *65* (1), 315−499.

(7) Janssens, S.; Van den Mooter, G. Review: Physical Chemistry of Solid Dispersions. *J. Pharm. Pharmacol.* **2009**, *61* (12), 1571−1586.

(8) Mishra, D. K.; Dhote, V.; Bhargava, A.; Jain, D. K.; Mishra, P. K. Amorphous Solid Dispersion Technique for Improved Drug Delivery: Basics to Clinical Applications. *Drug Delivery Transl. Res.* **2015**, *5* (6), 552−565.

(9) Li, J.; Patel, D.; Wang, G. Use of Spray-Dried Dispersions in Early Pharmaceutical Development: Theoretical and Practical Challenges. *AAPS J.* **2017**, *19* (2), 321−333.

(10) Wyttenbach, N.; Kuentz, M. Glass-Forming Ability of Compounds in Marketed Amorphous Drug Products. *Eur. J. Pharm. Biopharm.* **2017**, *112*, 204−208.

(11) Davis, M.; Walker, G. Recent Strategies in Spray Drying for the Enhanced Bioavailability of Poorly Water-Soluble Drugs. *J. Controlled Release* **2018**, *269*, 110−127.

(12) Hiew, T. N.; Zemlyanov, D. Y.; Taylor, L. S.; Pharmacy, P.; Lafayette, W.; States, U.; Lafayette, W. Balancing Solid-State Stability and Dissolution Performance of Lumefantrine Amorphous Solid Dispersions: The Role of Polymer Choice and Drug-Polymer Interactions. *Mol. Pharm.* **2021**, *19* (2), 392−413.

(13) Saboo, S.; Kestur, U. S.; Flaherty, D. P.; Taylor, L. S. Congruent Release of Drug and Polymer from Amorphous Solid Dispersions: Insights into the Role of Drug-Polymer Hydrogen Bonding, Surface Crystallization, and Glass Transition. *Mol. Pharmaceutics* **2020**, *17* (4), 1261−1275.

(14) Sun, C. C. Materials Science Tetrahedron—A Useful Tool for Pharmaceutical Research and Development. *J. Pharm. Sci.* **2009**, *98* (5), 1671−1687.

(15) Ricarte, R. G.; Li, Z.; Johnson, L. M.; Ting, J. M.; Reineke, T. M.; Bates, F. S.; Hillmyer, M. A.; Lodge, T. P. Direct Observation of Nanostructures during Aqueous Dissolution of Polymer/Drug Particles. *Macromolecules* **2017**, *50* (8), 3143−3152.

(16) Van Zee, N. J.; Hillmyer, M. A.; Lodge, T. P. Role of Polymer Excipients in the Kinetic Stabilization of Drug-Rich Nanoparticles. *ACS Appl. Bio Mater.* **2020**, *3* (10), 7243−7254.

(17) Bonnett, P. E.; Carpenter, K. J.; Dawson, S.; Davey, R. J. Solution Crystallisation via a Submerged Liquid—Liquid Phase Boundary: Oiling Out. *Chem. Commun.* **2003**, No. 6, 698−699.

(18) Vekilov, P. G. Dense Liquid Precursor for the Nucleation of Ordered Solid Phases from Solution. *Cryst. Growth Des.* **2004**, *4* (4), 671−685.

(19) Erdemir, D.; Lee, A. Y.; Myerson, A. S. Nucleation of Crystals from Solution: Classical and Two-Step Models. *Acc. Chem. Res.* **2009**, *42* (5), 621−629.

(20) Ilevbare, G. A.; Taylor, L. S. Liquid—Liquid Phase Separation in Highly Supersaturated Aqueous Solutions of Poorly Water-Soluble Drugs: Implications for Solubility Enhancing Formulations. *Cryst. Growth Des.* **2013**, *13* (4), 1497−1509.

(21) Taylor, L. S.; Zhang, G. G. Z. Physical Chemistry of Supersaturated Solutions and Implications for Oral Absorption. *Adv. Drug Delivery Rev.* **2016**, *101*, 122−142.

(22) Yang, R.; Mann, A. K. P.; Van Duong, T.; Ormes, J. D.; Okoh, G. A.; Hermans, A.; Taylor, L. S. Drug Release and Nanodroplet Formation from Amorphous Solid Dispersions: Insight into the Roles of Drug Physicochemical Properties and Polymer Selection. *Mol. Pharmaceutics* **2021**, *18* (5), 2066−2081.

(23) Ricarte, R. G.; Van Zee, N. J.; Li, Z.; Johnson, L. M.; Lodge, T. P.; Hillmyer, M. A. Recent Advances in Understanding the Micro- and Nanoscale Phenomena of Amorphous Solid Dispersions. *Mol. Pharmaceutics* **2019**, *16* (10), 4089−4103.

(24) Mosquera-Giraldo, L. I.; Li, N.; Wilson, V. R.; Nichols, B. L. B.; Edgar, K. J.; Taylor, L. S. Influence of Polymer and Drug Loading on the Release Profile and Membrane Transport of Telaprevir. *Mol. Pharmaceutics* **2018**, *15* (4), 1700−1713.

(25) Indulkar, A. S.; Lou, X.; Zhang, G. G. Z.; Taylor, L. S. Insights into the Dissolution Mechanism of Ritonavir-Copovidone Amorphous Solid Dispersions: Importance of Congruent Release for Enhanced Performance. *Mol. Pharmaceutics* **2019**, *16* (3), 1327−1339.

(26) Ting, J. M.; Tale, S.; Purchel, A. A.; Jones, S. D.; Widanapathirana, L.; Tolstyka, Z. P.; Guo, L.; Guillaudeu, S. J.; Bates, F. S.; Reineke, T. M. High-Throughput Excipient Discovery Enables Oral Delivery of Poorly Soluble Pharmaceuticals. *ACS Cent. Sci.* **2016**, *2* (10), 748−755.

(27) Turner, K.; Zhu, P. W.; Napper, D. H. Coil-to-Globule Transitions of Interfacial Copolymers in Better than Theta-Solvents. *Colloid Polym. Sci.* **1996**, *274* (7), 622−627.

(28) de Gennes, P. G. A Second Type of Phase Separation in Polymer Solutions. *C. R. Acad. Sc. Paris, Ser. II* **1991**, *313* (10), 1117−1122.

(29) Li, Z.; Van Zee, N. J.; Bates, F. S.; Lodge, T. P. Polymer Nanogels as Reservoirs to Inhibit Hydrophobic Drug Crystallization. *ACS Nano* **2019**, *13* (2), 1232−1243.

(30) Johnson, L. M.; Hillmyer, M. A. Critical Excipient Properties for the Dissolution Enhancement of Phenytoin. *ACS Omega* **2019**, *4* (21), 19116−19127.

(31) Johnson, L. M.; Li, Z.; LaBelle, A. J.; Bates, F. S.; Lodge, T. P.; Hillmyer, M. A. Impact of Polymer Excipient Molar Mass and End Groups on Hydrophobic Drug Solubility Enhancement. *Macromolecules* **2017**, *50* (3), 1102−1112.

(32) Li, Z.; Johnson, L. M.; Ricarte, R. G.; Yao, L. J.; Hillmyer, M. A.; Bates, F. S.; Lodge, T. P. Enhanced Performance of Blended Polymer Excipients in Delivering a Hydrophobic Drug through the Synergistic Action of Micelles and HPMCAS. *Langmuir* **2017**, *33* (11), 2837−2848.

(33) Li, Z.; Lenk, T. I.; Yao, L. J.; Bates, F. S.; Lodge, T. P. Maintaining Hydrophobic Drug Supersaturation in a Micelle Corona Reservoir. *Macromolecules* **2018**, *51* (2), 540−551.

(34) Ohnsorg, M. L.; Prendergast, P. C.; Robinson, L. L.; Bockman, M. R.; Bates, F. S.; Reineke, T. M. Bottlebrush Polymer Excipients Enhance Drug Solubility: Influence of End-Group Hydrophilicity and Thermoresponsiveness. *ACS Macro Lett.* **2021**, *10* (3), 375−381.

(35) Reineke, T.; Bates, F. S.; Ohnsorg, M. Macromonomers and Bottle Brush Polymers for Delivery of Biological Agents. U.S. Patent 20,220,339,288 A1, 2022.

(36) Genentech, Inc. *A Study of GDC-0810 versus Fulvestrant in Postmenopausal Women with Advanced or Metastatic Breast Cancer Resistant to Aromatase Inhibitor (AI) Therapy (HydranGea)*, 2021; Vol. NCT0256980.

(37) Joseph, J. D.; Darimont, B.; Zhou, W.; Arrazate, A.; Young, A.; Ingalla, E.; Walter, K.; Blake, R. A.; Nonomiya, J.; Guan, Z.; Kategaya, L.; Govek, S. P.; Lai, A. G.; Kahraman, M.; Brigham, D.; Sensintaffar, J.; Lu, N.; Shao, G.; Qian, J.; Grillot, K.; Moon, M.; Prudente, R.; Bischoff, E.; Lee, K. J.; Bonnefous, C.; Douglas, K. L.; Julien, J. D.; Nagasawa, J. Y.; Aparicio, A.; Kaufman, J.; Haley, B.; Giltnane, J. M.; Wertz, I. E.; Lackner, M. R.; Nannini, M. A.; Sampath, D.; Schwarz, L.; Manning, H. C.; Tantawy, M. N.; Arteaga, C. L.; Heyman, R. A.; Rix, P. J.; Friedman, L.; Smith, N. D.; Metcalfe, C.; Hager, J. H. The Selective Estrogen Receptor Downregulator GDC-0810 Is Efficacious in Diverse Models of ER+ Breast Cancer. *Elife* **2019**, *8*, No. e44851.

(38) Lai, A.; Kahraman, M.; Govek, S.; Nagasawa, J.; Bonnefous, C.; Julien, J.; Douglas, K.; Sensintaffar, J.; Lu, N.; Lee, K. J.; Aparicio, A.; Kaufman, J.; Qian, J.; Shao, G.; Prudente, R.; Moon, M. J.; Joseph, J. D.; Darimont, B.; Brigham, D.; Grillot, K.; Heyman, R.; Rix, P. J.; Hager, J. H.; Smith, N. D. Identification of GDC-0810 (ARN-810), an Orally Bioavailable Selective Estrogen Receptor Degrader (SERD) That Demonstrates Robust Activity in Tamoxifen-Resistant Breast Cancer Xenografts. *J. Med. Chem.* **2015**, *58* (12), 4888–4904.

(39) Bardia, A.; Mayer, I.; Winer, E.; Linden, H. M.; Ma, C. X.; Parker, B. A.; Bellet, M.; Arteaga, C. L.; Cheeti, S.; Gates, M.; Chang, C.-W.; Fredrickson, J.; Spoerke, J. M.; Moore, H. M.; Giltnane, J.; Friedman, L. S.; Chow Maneval, E.; Chan, I.; Jhaveri, K. The Oral Selective Estrogen Receptor Degrader GDC—0810 (ARN—810) in Postmenopausal Women with Hormone Receptor—Positive HER2— Negative (HR +/HER2 -) Advanced/Metastatic Breast Cancer. *Breast Cancer Res. Treat.* **2023**, *197* (2), 319–331.

(40) McDonnell, D. P.; Wardell, S. E.; Norris, J. D. Oral Selective Estrogen Receptor Downregulators (SERDs), a Breakthrough Endocrine Therapy for Breast Cancer. *J. Med. Chem.* **2015**, *58* (12), 4883–4887.

(41) Hou, H. H.; Jia, W.; Liu, L.; Cheeti, S.; Li, J.; Nauka, E.; Nagapudi, K. Effect of Microenvironmental PH Modulation on the Dissolution Rate and Oral Absorption of the Salt of a Weak Acid— Case Study of GDC-0810. *Pharm. Res.* **2018**, *35* (2), 37.

(42) Wilson, V. R.; Mugheirbi, N. A.; Mosquera-Giraldo, L. I.; Deac, A.; Moseson, D. E.; Smith, D. T.; Novo, D. C.; Borca, C. H.; Slipchenko, L. V.; Edgar, K. J.; Taylor, L. S. Interaction of Polymers with Enzalutamide Nanodroplets—Impact on Droplet Properties and Induction Times. *Mol. Pharmaceutics* **2021**, *18* (3), 836–849.

(43) Correa-soto, C. E.; Gao, Y.; Indulkar, A. S.; Zhang, G. G. Z.; Taylor, L. S.; Zhang, E. G. G. G. Z.; Taylor, L. S. Role of Surfactants in Improving Release from Higher Drug Loading Amorphous Solid Dispersions. *Int. J. Pharm.* **2022**, *625*, 122120.

(44) Metz, G.; Wu, X.; Smith, S. O. Ramped-Amplitude Cross Polarization in Magic-Angle Spinning NMR. *J. Magn. Reson. Ser. A* **1994**, *110* (2), 219–227.

(45) Pines, A.; Gibby, M. G.; Waugh, J. S. Proton-Enhanced Nuclear Induction Spectroscopy. a Method for High Resolution Nmr of Dilute Spins in Solids. *J. Chem. Phys.* **1972**, *56* (4), 1776–1777.

(46) Stejskal, E. O.; Schaefer, J.; Waugh, J. S. Magic-Angle Spinning and Polarization Transfer in Proton-Enhanced NMR. *J. Magn. Reson.* **1977**, *28* (1), 105–112.

(47) Fung, B. M.; Khitrin, A. K.; Ermolaev, K. An Improved Broadband Decoupling Sequence for Liquid Crystals and Solids. *J. Magn. Reson.* **2000**, *142* (1), 97–101.

(48) Dixon, W. T. Spinning-Sideband-Free and Spinning Sideband-Only NMR Spectra in Spinning Samples. *J. Chem. Phys.* **1982**, *77* (4), 1800–1809.

(49) Song, Z.; Antzutkin, O. N.; Feng, X.; Levitt, M. H. Sideband Suppression in Magic-Angle-Spinning NMR by a Sequence of 5 π Pulses. *Solid State Nucl. Magn. Reson.* **1993**, *2* (3), 143–146.

(50) Yin, L.; Hillmyer, M. A. Preparation and Performance of Hydroxypropyl Methylcellulose Esters of Substituted Succinates for in Vitro Supersaturation of a Crystalline Hydrophobic Drug. *Mol. Pharmaceutics* **2014**, *11* (1), 175–185.

(51) Paudel, A.; Worku, Z. A.; Meeus, J.; Guns, S.; Van den Mooter, G. Manufacturing of Solid Dispersions of Poorly Water Soluble Drugs

by Spray Drying: Formulation and Process Considerations. *Int. J. Pharm.* **2013**, *453* (1), 253–284.

(52) Pham, P. D.; Monge, S.; Lapinte, V.; Raoul, Y.; Robin, J. J. Various Radical Polymerizations of Glycerol-Based Monomers. *Eur. J. Lipid Sci. Technol.* **2013**, *115* (1), 28–40.

(53) Bühler, V. *Kollidon Polyvinylpyrrolidone Excipients for the Pharmaceutical Industry*, 9th ed.; BASF SE: Ludwigshafen, Germany, 2008.

(54) Taghizadeh, M. T.; Foroutan, M. Water-Soluble Copolymers of N-Vinylpyrrolidone and Vinyl Acetate: Synthesis, Characterization, and Monomer Reactivity at High Conversions. *J. Polym. Res.* **2004**, *11* (3), 203–209.

(55) Atanase, L. I.; Winninger, J.; Delaite, C.; Riess, G. Reversible Addition—Fragmentation Chain Transfer Synthesis and Micellar Characteristics of Biocompatible Amphiphilic Poly (Vinyl Acetate)— Graft -Poly (N -Vinyl-2-Pyrrolidone) Copolymers. *Eur. Polym. J.* **2014**, *53*, 109–117.

(56) Nese, A.; Li, Y.; Averick, S.; Kwak, Y.; Konkolewicz, D.; Sheiko, S. S.; Matyjaszewski, K. Synthesis of Amphiphilic Poly(N-Vinyl-pyrrolidone)-b-Poly(Vinyl Acetate) Molecular Bottlebrushes. *ACS Macro Lett.* **2012**, *1* (1), 227–231.

(57) Ohnsorg, M. L.; Ting, J. M.; Jones, S. D.; Jung, S.; Bates, F. S.; Reineke, T. M. Tuning PNIPAm Self-Assembly and Thermoresponse: Roles of Hydrophobic End-Groups and Hydrophilic Comonomer. *Polym. Chem.* **2019**, *10* (25), 3469–3479.

(58) Zhang, W.; Haser, A.; Hou, H. H.; Nagapudi, K. Evaluation of Accuracy of Amorphous Solubility Advantage Calculation by Comparison with Experimental Solubility Measurement in Buffer and Biorelevant Media. *Mol. Pharmaceutics* **2018**, *15* (4), 1714–1723.

(59) Martínez-Landeira, P.; Ruso, J. M.; Prieto, G.; Sarmiento, F. Surface Tensions, Critical Micelle Concentrations, and Standard Free Energies of Micellization of C8-Lecithin at Different PHs and Electrolyte Concentrations. *J. Chem. Eng. Data* **2002**, *47* (4), 1017–1021.

(60) Hou, H. H.; Rajesh, A.; Pandya, K. M.; Lubach, J. W.; Muliadi, A.; Yost, E.; Jia, W.; Nagapudi, K. Impact of Method of Preparation of Amorphous Solid Dispersions on Mechanical Properties: Comparison of Coprecipitation and Spray Drying. *J. Pharm. Sci.* **2019**, *108* (2), 870–879.

(61) Ting, J. M.; Navale, T. S.; Jones, S. D.; Bates, F. S.; Reineke, T. M. Deconstructing HPMCAS: Excipient Design to Tailor Polymer-Drug Interactions for Oral Drug Delivery. *ACS Biomater. Sci. Eng.* **2015**, *1* (10), 978–990.

(62) Curatolo, W.; Nightingale, J. A.; Herbig, S. M. Utility of Hydroxypropylmethylcellulose Acetate Succinate (HPMCAS) for Initiation and Maintenance of Drug Supersaturation in the GI Milieu. *Pharm. Res.* **2009**, *26* (6), 1419–1431.

(63) Friesen, D. T.; Shanker, R.; Crew, M.; Smithey, D. T.; Curatolo, W. J.; Nightingale, J. A. S. Hydroxypropyl Methylcellulose Acetate Succinate-Based Spray-Dried Dispersions: An Overview. *Mol. Pharmaceutics* **2008**, *5* (6), 1003–1019.

(64) Ting, J. M.; Navale, T. S.; Bates, F. S.; Reineke, T. M. Precise Compositional Control and Systematic Preparation of Multimono-meric Statistical Copolymers. *ACS Macro Lett.* **2013**, *2* (9), 770–774.

(65) Ting, J. M.; Navale, T. S.; Bates, F. S.; Reineke, T. M. Design of Tunable Multicomponent Polymers As Modular Vehicles to Solubilize Highly Lipophilic Drugs. *Macromolecules* **2014**, *47* (19), 6554–6565.

(66) Schittny, A.; Philipp-Bauer, S.; Detampel, P.; Huwyler, J.; Puchkov, M. Mechanistic Insights into Effect of Surfactants on Oral Bioavailability of Amorphous Solid Dispersions. *J. Controlled Release* **2020**, *320*, 214–225.

(67) Chen, J.; Ormes, J. D.; Higgins, J. D.; Taylor, L. S. Impact of Surfactants on the Crystallization of Aqueous Suspensions of Celecoxib Amorphous Solid Dispersion Spray Dried Particles. *Mol. Pharmaceutics* **2015**, *12* (2), 533–541.

(68) Solanki, N. G.; Lam, K.; Tahsin, M.; Gumaste, S. G.; Shah, A. V.; Serajuddin, A. T. M. Effects of Surfactants on Itraconazole-HPMCAS Solid Dispersion Prepared by Hot-Melt Extrusion I:

Miscibility and Drug Release. *J. Pharm. Sci.* **2019**, *108* (4), 1453−1465.

(69) Kutnyanszky, E.; Embrechts, A.; Hempenius, M. A.; Vancso, G. J. Is There a Molecular Signature of the LCST of Single PNIPAM Chains as Measured by AFM Force Spectroscopy? *Chem. Phys. Lett.* **2012**, *535*, 126−130.

(70) Abdel Azim, A.-A. A.; Tenhu, H.; Maerta, J.; Sundholm, F. Flexibility and Hydrodynamic Properties of Poly (Vinylpyrrolidone) in Non-Ideal Solvents. *Polym. Bull.* **1992**, *29* (3−4), 461−467.

(71) Fetters, L. J.; Lohse, D. J.; Richter, D.; Witten, T. A.; Zirkel, A. Connection between Polymer Molecular Weight, Density, Chain Dimensions, and Melt Viscoelastic Properties. *Macromolecules* **1994**, *27* (17), 4639−4647.

(72) Lodge, T.; Hiemenz, P. *Polymer Chemistry*, 3rd ed.; Taylor and Francis Group, 2020.

(73) Zhang, X.; Liu, C.; Wang, Z. Force Spectroscopy of Polymers: Studying on Intramolecular and Intermolecular Interactions in Single Molecular Level. *Polymer* **2008**, *49* (16), 3353−3361.